MATERIALS SCIENCE

Bioresponsive nano-antibacterials for H_2S-sensitized hyperthermia and immunomodulation against refractory implant–related infections

Zheng Su[1]†, Lingtong Kong[1]†, Yong Dai[1]†, Jin Tang[2]*, Jiawei Mei[1], Zhengzheng Qian[3], Yuanyuan Ma[4], Qianming Li[1], Shenghong Ju[4], Jiaxing Wang[5]*, Wenpei Fan[3]*, Chen Zhu[1]*

There is an increasingly growing demand for nonantibiotic strategies to overcome drug resistance in bacterial biofilm infections. Here, a novel "gas-sensitized hyperthermia" strategy is proposed for appreciable bacteria killing by the smart design of a metal-organic framework (MOF)–sealed Prussian blue–based nanocarrier (MSDG). Once the biofilm microenvironment (BME) is reached, the acidity-activated MOF degradation allows the release of diallyl trisulfide and subsequent glutathione-responsive generation of hydrogen sulfide (H_2S) gas. Upon near-infrared irradiation, H_2S-sensitized hyperthermia arising from MSDG can efficiently eliminate biofilms through H_2S-induced extracellular DNA damage and heat-induced bacterial death. The generated H_2S in the biofilm can stimulate the polarization of macrophages toward M2 phenotype for reshaping immune microenvironment. Subsequently, the secretion of abundant regeneration-related cytokines from M2 macrophages accelerates tissue regeneration by reversing the infection-induced pro-inflammatory environment in an implant-related infection model. Collectively, such BME-responsive nano-antibacterials can achieve biofilm-specific H_2S-sensitized thermal eradiation and immunomodulatory tissue remodeling, thus realizing the renaissance of precision treatment of refractory implant–related infections.

INTRODUCTION

Bacterial biofilm infections threaten the health care system and human welfare and continue to cause some of the most severe diseases, such as implant-related infections, septic arthritis, and dermatosis, resulting in approximately 17 million deaths worldwide every year (*1*–*4*). Even worse, the abuse of antibiotics has aggravated the emergence of drug resistance in many pathogens (*5*, *6*). Refractory biofilm infections and evolution of multidrug resistance are responsible for chronic inflammation and the failure of implant surgery (*4*, *7*). In natural and clinical settings, most bacteria tend to irreversibly adhere to the surface of implants or tissues and transform into self-produced extracellular polymeric substances (EPSs), which are known as biofilms. Biofilms can create localized and protected microenvironments (*8*–*11*). The EPS typically consists of extracellular DNA (eDNA), polysaccharides, and proteins. The encapsulation of EPS creates a hypoxic, acidic (pH ~5.5), and reductive overexpressed glutathione (GSH) microenvironment in biofilms, such as *Escherichia coli* and methicillin-resistant *Staphylococcus aureus* (MRSA) biofilm (*12*–*17*). As a physical/chemical barrier, EPS can not only prohibit the infiltration of the traditional antibiotic but also hinder host immune responses, thus resulting in the failure of antibacterial therapy and eventually causing chronic/obstinate infections (*5*, *8*, *18*). Therefore, the exploration of other more biocompatible and effective therapeutic strategies is of utmost priority to treat bacterial biofilm infections with minimal side effects.

As an alternative to antibiotics, gasotransmitters [e.g., hydrogen sulfide (H_2S), nitric oxide (NO), and carbon monoxide (CO)] are emerging as a "green drug" for effective gas therapy of various diseases (*19*–*22*). Gas therapy is usually combined with other treatments to strengthen antibacterial efficacy. For example, some researchers reported that the synergy of NO gas and near-infrared (NIR)–excited phototherapy (e.g., photothermal therapy and photodynamic therapy) exhibited strong antibacterial/antibiofilm activity mainly via NO-mediated DNA damage (*23*–*25*). Other researchers such as Li *et al.* (*26*) have demonstrated the potential of NO-activated M1 macrophage-associated immunotherapy to eradicate MRSA biofilms on bone implants. The anti-inflammatory features of CO and NO could mitigate the inflammation-related reaction during the antibiofilm process (*25*, *27*). It is noteworthy that H_2S not only possesses the merits of NO and CO but also can stimulate the M2 macrophage polarization (*19*, *28*–*32*). For instance, Hoffman *et al.* (*29*) pointed out that H_2S was a DNA-damaging mutagen. Li *et al.* (*30*) reported the H_2S-promoted anti-inflammatory effect. Wu *et al.* (*31*) revealed H_2S-stimulated M2 macrophage polarization. Therefore, H_2S exhibits the advantage of improving the therapeutic effects and reducing the adverse effects of hyperthermia for thorough biofilm elimination. To the best of our knowledge, very few researchers have reported the synergistic use of H_2S gas and hyperthermia to achieve biofilm elimination and simultaneous macrophage-associated immunomodulation. With regards to unrestrained H_2S gas release, many bioresponsive donors have been investigated to achieve a more regulated and monitored release of H_2S (*33*, *34*). Here, we introduce a reducibility-responsive H_2S donor, diallyl trisulfide (DATS), which

[1]Department of Orthopedics, The First Affiliated Hospital of USTC, Division of Life Sciences and Medicine, University of Science and Technology of China, Hefei, Anhui 230001, China. [2]Department of Clinical Laboratory, Shanghai Jiao Tong University Affiliated Sixth People's Hospital, Shanghai Jiao Tong University, Shanghai 200233, China. [3]State Key Laboratory of Natural Medicines and Jiangsu Key Laboratory of Drug Discovery for Metabolic Diseases, Center of Advanced Pharmaceuticals and Biomaterials, China Pharmaceutical University, Nanjing 210009, China. [4]Jiangsu Key Laboratory of Molecular and Functional Imaging, Department of Radiology, Zhongda Hospital, Medical School of Southeast University, 87 DingJiaQiao Road, Nanjing 210009, China. [5]Department of Orthopaedics, Shanghai Jiao Tong University Affiliated Sixth People's Hospital, Shanghai Jiao Tong University, Shanghai 200233, China.
*Corresponding author. Email: tangjin6ph@126.com (J.T.); jxwang@shsmu.edu.cn (J.W.); wenpei.fan@cpu.edu.cn (W.F.); zhuchena@ustc.edu.cn (C.Z.)
†These authors contributed equally to this work.

can rapidly react with GSH within biofilm microenvironment (BME) to generate H_2S gas, therefore circumventing the problem of spontaneous and unwanted H_2S release in unaffected tissues (*35*, *36*). Besides, the BME-responsive H_2S generation is also heavily reliant on the bioavailability of DATS, which undermines the assistance of smart yet powerful nanocarriers in biofilm-specific DATS delivery.

Prussian blue (PB) nanoparticles have shown remarkable biocompatibility and negligible cytotoxicity and hence is clinically approved by the U.S. Food and Drug Administration (*37*). Because of its strong absorption in the NIR region, PB has been extensively used for NIR-activated hyperthermia and photoacoustic imaging (PAI) (*38*). Further doping of Gd ions into PB can enhance the magnetic resonance imaging (MRI) contrast. The dual-modal MRI/PAI of Gd-doped PB (GPB) has the merits of high spatial resolution, high sensitivity, and deep tissue permeability (*39*, *40*), which is beneficial for precise location of biofilms and real-time imaging monitoring. One of the greatest advantages of GPB is its ability to encapsulate drugs in its porous structure. However, the spontaneous or off-target drug release remains a challenging issue for PB-based nanocarriers, which requires the development of gatekeepers to block the pore channels of PB to prevent premature drug leakage. Once the target is reached, the gatekeepers should respond selectively to the endogenous or exogenous stimuli of the target and reopen the pores to precisely regulate the on-demand drug release.

In this study, we report the perceptive use of MOF as an acidity-responsive gatekeeper to seal the pore channels of GPB. After preloading DATS into GPB, a novel "bottle-in-a-ship" strategy is first applied to seal MOF inside the pore channels of GPB (denoted as MSDG). In neutral tissues, MOF is stable and thus prevents leakage of DATS from GPB. Upon reaching the biofilm, MOF is decomposed in response to the acidic BME, allowing the release of DATS. The released DATS can further react with the overexpressed GSH within the reductive BME to generate H_2S gas. This ultimately leads to the on-target release of H_2S gas for precise gas therapy to break eDNA inside biofilms. Assisted by the heat flow generated from NIR-irradiated GPB, the judiciously designed MSDG can give rise to H_2S-sensitized hyperthermia to eliminate most biofilms. The exploitation of BME-responsive H_2S release marks the beginning of precise biofilm-specific gas therapy for considerably lowering the temperature threshold for hyperthermia, thereby minimizing any potential collateral thermal damage to unaffected tissues and ensuring the safety of the entire treatment process. Our study reveals that the MSDG-mediated M2 macrophage polarization can promote the reversing of infection-induced pro-inflammatory environment. The secretion of abundant regeneration-related cytokines accelerates the tissue remodeling after eliminating biofilms, which is beneficial for combating against refractory implant–related infections (Fig. 1). We believe that this study may not only illuminate guidelines for the design of BME-responsive MOF-sealed heterostructure nanocarriers but also shed light on the development of other BME-activated synergistic gas treatment paradigms for proficient biofilm elimination.

RESULTS AND DISCUSSION

Synthesis and characterization of PB

Mesoporous PB nanoparticles were prepared using a facile "hydrothermal method" by mixing the iron precursor ($K_3[Fe(CN)_6]$) and polyvinyl pyrrolidone (PVP) under hydrothermal conditions (80°C). During the synthesis, the morphology and size of PB were adjusted by modulating the feeding HCl concentration. With the gradual decrease in HCl concentration, the morphology of PB nanoparticles changed from spherical to cubic (Fig. 2, A to D), and both the actual and hydrolyzed particle sizes of PB were enlarged (Fig. 2, E to H, and fig. S1). The lower HCl concentration resulted in the generation of less formative Fe ions and larger PB sizes. HCl tended to etch more edges of PB, so the morphology of PB could be modulated from square to round by increasing the feeding HCl concentration (*41*, *42*). The Fourier transform infrared (FTIR) spectra of PB showed the characteristic band of Fe-C≡N-Fe ferricyanide stretching vibration at 2080 cm^{-1} (fig. S2), which confirmed the successful formation of PB nanoparticles. It was observed that the enlarged particle size could decrease the 2080 cm^{-1} band intensity and therefore restrict the stretching vibration of Fe-C≡N-Fe ferricyanide in the PB structure.

Photothermal conversion and PAI of PB

Because of its strong NIR absorption, PB exhibited excellent photothermal conversion upon NIR (808 nm) laser irradiation. Among the four PB (I, II, III, and IV) nanoparticles prepared, PB-II demonstrated the strongest absorbance at 808 nm (Fig. 2I) and had the highest temperature (up to 65.4°C) after 5 min of NIR laser irradiation (Fig. 2J). On the contrary, the temperature of deionized (DI) water showed no significant change upon NIR laser irradiation. This suggested that PB-II exhibited the best photothermal conversion among all the PB nanoparticles prepared. Considering the relatively small particle size (123.32 ± 18.37 nm; Fig. 2F), uniform spherical morphology (Fig. 2B), and the best photothermal conversion (Fig. 2J), PB-II was selected as the most suitable candidate for further experiments.

PB-II was subjected to recurrent heating and cooling experiments to evaluate its photothermal reversibility. High photothermal stability was observed after six cycles of NIR laser irradiation, suggesting promising photothermal reversibility of PB-II for durable and repeated photothermal applications without affecting its functionality (Fig. 2K). Meanwhile, we also observed that the photothermal effect of PB-II was dependent on various factors such as its concentration, NIR laser power density, and irradiation time (fig. S3). According to the formula and taking the related parameters into account (fig. S4 and table S1), the photothermal conversion efficiency (PTCE; η) of PB-II was calculated to be 61.8% (Fig. 2L). Moreover, PB-II also exhibited concentration-dependent photoacoustic (PA) values within the NIR range of 680 to 970 nm, implying that PB-II could act as an outstanding contrasting agent for amplifying the PAI signal (Fig. 2, M and N).

Synthesis and characterization of GPB

To endow PB with MRI contrast, Gd ion was doped into the crystal lattice of PB-II to produce GPB nanoparticles. By varying the feeding $Gd(NO_3)_3$ concentration while maintaining the same feeding HCl concentration of 0.1 M, four types of GPB (I, II, III, and IV) were synthesized with varied Gd/Fe mass ratios. With the elevated feeding concentration of $Gd(NO_3)_3$, the Gd/Fe mass ratio gradually increased from 0.01191 to 0.02943 (table S2). Compared with PB-II, the particle sizes of all GPB (I, II, III, and IV) were augmented, but their spherical morphology remained unperturbed (Fig. 3, A to H). The underlying mechanism resulting in the enlarged particle size of GPB might be attributed to the incorporation of Gd ions, which distorted the crystal lattice and changed the interatomic coupling

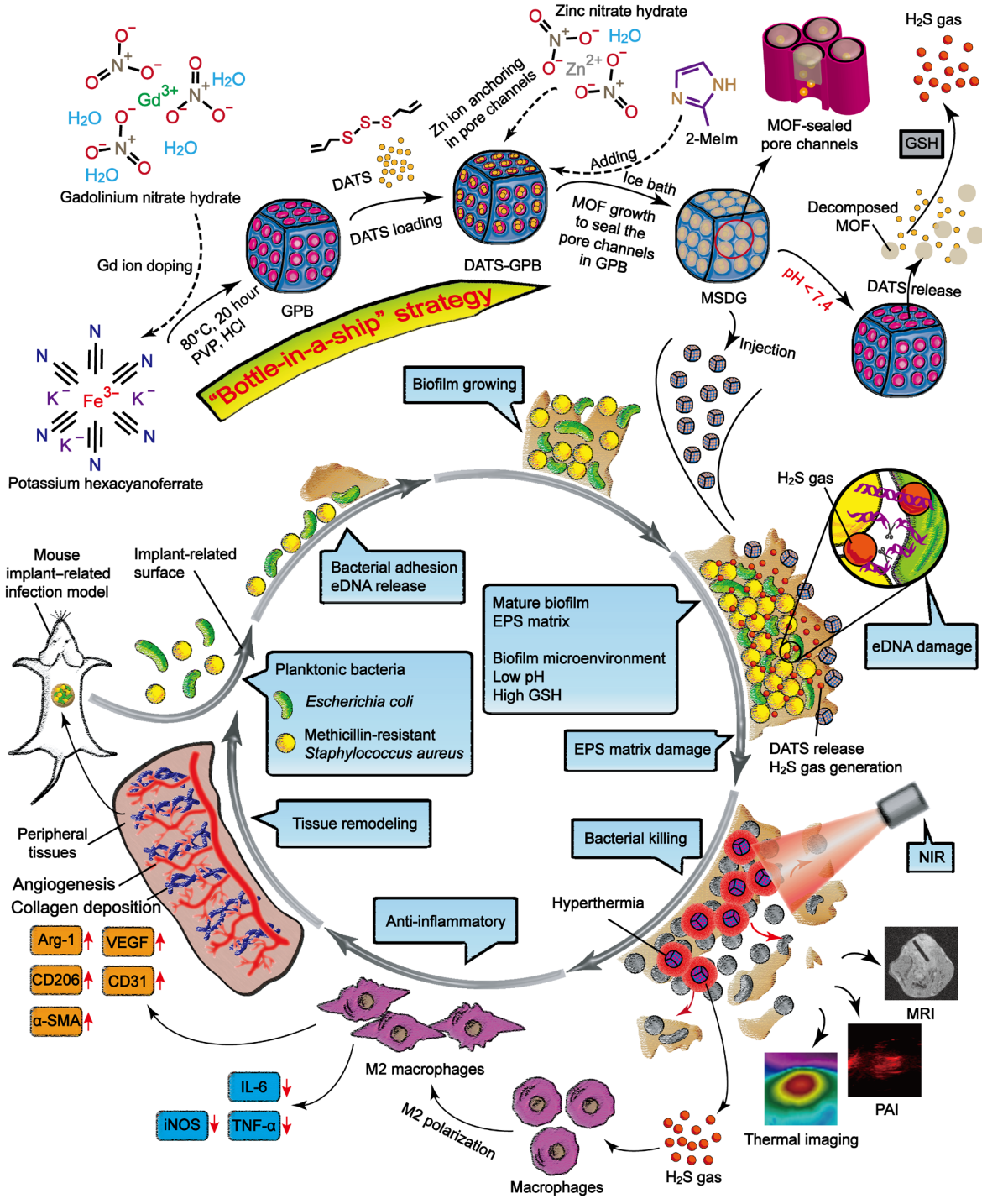

Fig. 1. Schematic illustration of design, synthesis, and biomedical applications of MSDG. MSDG is prepared by a bottle-in-a-ship strategy after loading DATS into GPB. Once MSDG reaches the biofilm, the degradation of MOF opens the gate and allows the release of DATS. The released DATS can further react with the overexpressed GSH within the reducing BME to generate H_2S gas. Assisted by the heat flow generated from NIR laser–irradiated GPB, H_2S gas can sensitize hyperthermia to achieve the efficient biofilm elimination with potential multimodal diagnosis application. Furthermore, MSDG-mediated immunomodulatory effects on M2 macrophage polarization inhibit infection-induced secretion of pro-inflammatory cytokines and establish a favorable immune microenvironment to promote tissue remodeling.

effects, thereby affecting the stability of the crystallographic process during the formation of PB (*43*). Similar to PB-II, all four GPB (I, II, III, and IV) nanoparticles exhibited high crystallinity, as depicted in their x-ray diffraction (XRD) patterns (fig. S5A). The characteristic peak at 15.5° (marked by stellate signs) corresponded to the (111) diffraction plane of gadolinium hexacynoferrate, indicating the covalent bond of Gd ions to the cyanide ligands in the crystal lattice of PB. In addition, characteristic bands at 2115 and 2024 cm^{-1} of

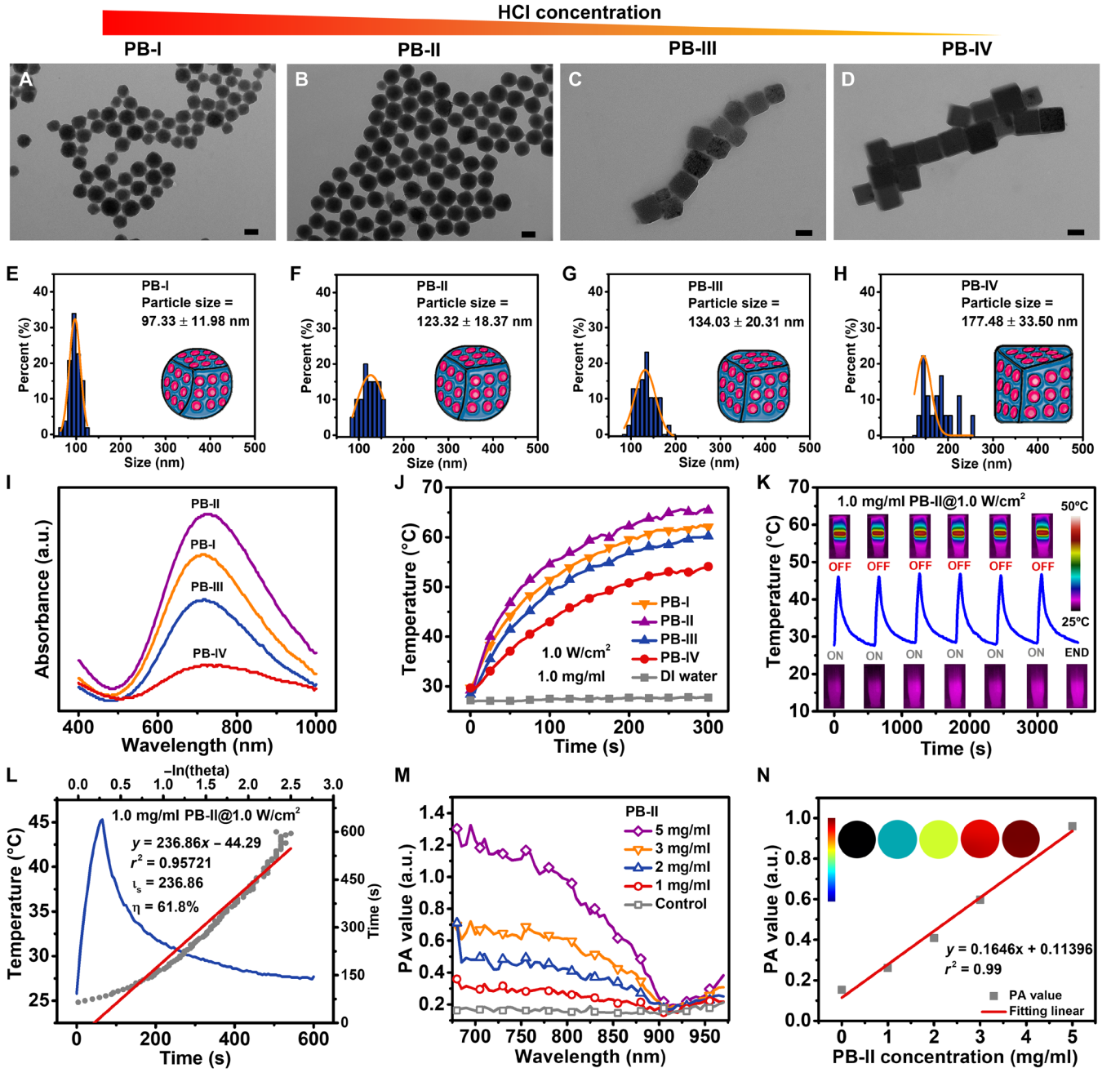

Fig. 2. Structure and performance of PB. (**A** to **D**) TEM images and (**E** to **H**) the corresponding particle size distributions of PB nanoparticles synthesized under varied pH values by varying the feeding HCl concentration. Scale bars, 100 nm. (**I** to **L**) Photothermal conversion of PB nanoparticles. (I) UV-Vis spectra of PB-I, PB-II, PB-III, and PB-IV. (J) Photothermal heating curves of PB-I, PB-II, PB-III, and PB-IV (1.0 mg/ml) upon 808-nm laser irradiation (1.0 W/cm^2). (K) Photothermal heating/cooling curves and thermographic images of PB-II (1.0 mg/ml) after six cycles of 808-nm laser irradiation (1.0 W/cm^2). (L) Plot of cooling time versus the negative natural logarithm of temperature driving force obtained from the cooling stage of PB-II. PTCE of PB-II is calculated to be 61.8%. (**M** and **N**) PAI performance of PB nanoparticles. (M) PA spectra of PB-II with varied concentrations. (N) Plot of PA value of PB-II at 808 nm versus concentration. Inset: Corresponding PAI images of PB-II with varied concentrations at 808 nm. a.u., arbitrary units.

typical gadolinium hexacynoferrate appeared in the FTIR spectra of GPB with elevated Gd/Fe mass ratios, validating the covalent integration of Gd ions within the crystal lattice of PB by forming the -Fe-C≡N-Gd- group (fig. S5B). The zeta potentials of the four GPB (I, II, III, and IV) nanoparticles were still negative (fig. S6), guaranteeing their efficient water dispersity.

MRI and photothermal conversion of GPB

Gd ion doping encouraged us to investigate the T_1-weighted MRI contrast performance of GPB. Proton T_1 relaxation measurements were performed to obtain the longitudinal relaxivity (r_1) value at a magnetic field of 7 T. As shown in Fig. 3 (I to L), the r_1 value of GPB-III derived from a linear fit of $1/T_1$ versus Gd ion concentration

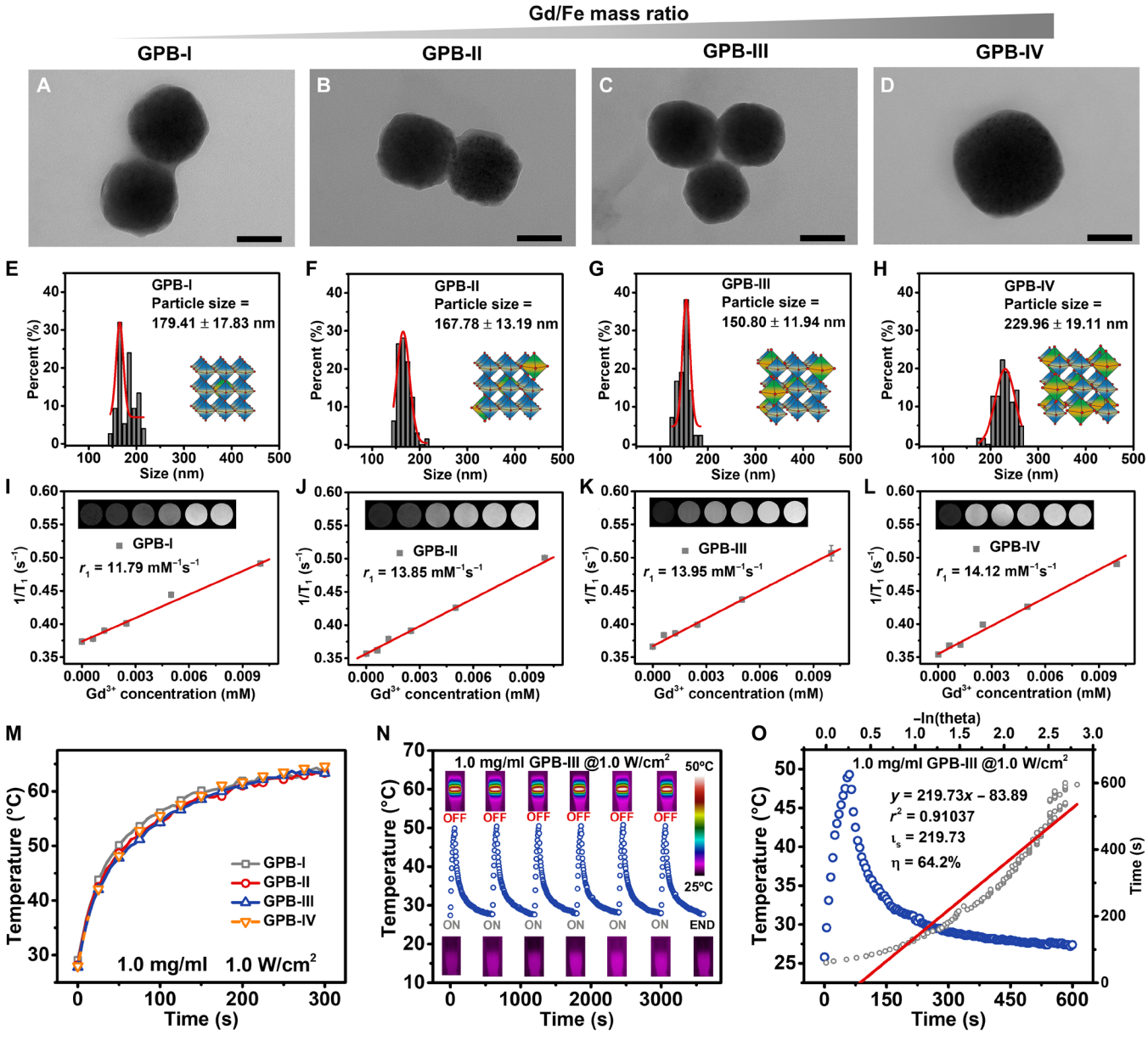

Fig. 3. Structure and performance of GPB. (**A** to **D**) TEM images, (**E** to **H**) particle size distributions, and (**I** to **L**) plots of $1/T_1$ versus Gd ion concentration for GPB-I, GPB-II, GPB-III, and GPB-IV with varied mass ratio of Gd/Fe by varying the feeding $Gd(NO_3)_3$ concentration. Magnetic field, 7 T. Scale bars, 100 nm. $n = 3$, means ± SD. (**M** to **O**) Photothermal conversion of GPB. (M) Photothermal heating curves of GPB-I, GPB-II, GPB-III, and GPB-IV (1.0 mg/ml) upon 808-nm laser irradiation (1.0 W/cm^2). (N) Photothermal heating/cooling curves and thermographic images of GPB-III (1.0 mg/ml) upon six cycles of 808-nm laser irradiation (1.0 W/cm^2). (O) Plot of cooling time versus the negative natural logarithm of temperature driving force obtained from the cooling stage of GPB-III. PTCE is calculated to be 64.2%.

was 13.95 mM^{-1} s^{-1}, which was higher than that of GPB-I and GPB-II, and even higher than that of the commercial contrast agent Magnevist (r_1 = 4.52 mM^{-1} s^{-1}). All four GPB (I, II, III, and IV) nanoparticles demonstrated similar photothermal heating curves upon NIR laser irradiation, indicating the negligible influence of Gd ion doping on the photothermal effect of GPB (Fig. 3M). GPB-III exhibited the smallest particle size (150.8 ± 11.94 nm) among GPB (I, II, III, and IV) despite the slightly lower r_1 value than GPB-IV. On the basis of this parameter, GPB-III was selected for further biomedical use. The element mapping images showed the uniform distribution of C, N, Fe, K, and Gd in GPB-III (fig. S7). GPB-III also demonstrated excellent photothermal stability and reversibility after six cycles of NIR laser irradiation (Fig. 3N). PTCE of GPB-III was estimated to be 64.2% (Fig. 3O, fig. S8, and table S3), which was slightly higher than that of PB (61.8%), further assuring the remarkable photothermal conversion of GPB-III (fig. S9).

Synthesis and characterization of the MOF-sealed GPB

The mesoporous structure of GPB (fig. S10A) can be successfully used for efficient drug loading and delivery. However, one of the drawbacks in this drug delivery method is that small drug molecules can easily leak if the pores are not blocked. Therefore, MOF (ZIF-8)

was chosen as the gatekeeper to seal GPB (denoted as MSG). The pore size and volume of MSG were substantially reduced compared to those of GPB (fig. S10), which implied that the pore sealing by MOF was effective in preventing premature and off-target drug leakage from GPB. Notably, a novel bottle-in-a-ship strategy was developed to synthesize MSG by just stepwise immersing GPB into a mixed solution containing a zinc source [$Zn(NO_3)_2$] and 2-methylimidazole (2-MeIm) for 15 min in an ice bath (Fig. 4A). This new synthetic bottle-in-a-ship methodology is defined as the introduction of MOF precursors into porous nanoparticles and subsequent transformation of the precursors to corresponding MOF inside the pore channels of the porous nanoparticles, eventually forming a MOF-sealed heterostructure. It was found that the MSG heterostructure could be attuned by modifying the ratio of the MOF precursors [$Zn(NO_3)_2$ and 2-MeIm] to GPB. When a high concentration of GPB reacted with low concentrations of $Zn(NO_3)_2$ and 2-MeIm, MOF thus formed, precipitated into the pore walls of GPB, and failed to completely seal the inner pore walls (fig. S11, A and B). With increasing concentrations of $Zn(NO_3)_2$ and 2-MeIm or decreasing concentration of GPB, there was an enhanced MOF formation resulting in complete filling of the pore channels, thereby effectively sealing the pore gates of GPB (Fig. 4B). The Zn/Fe mass ratio of

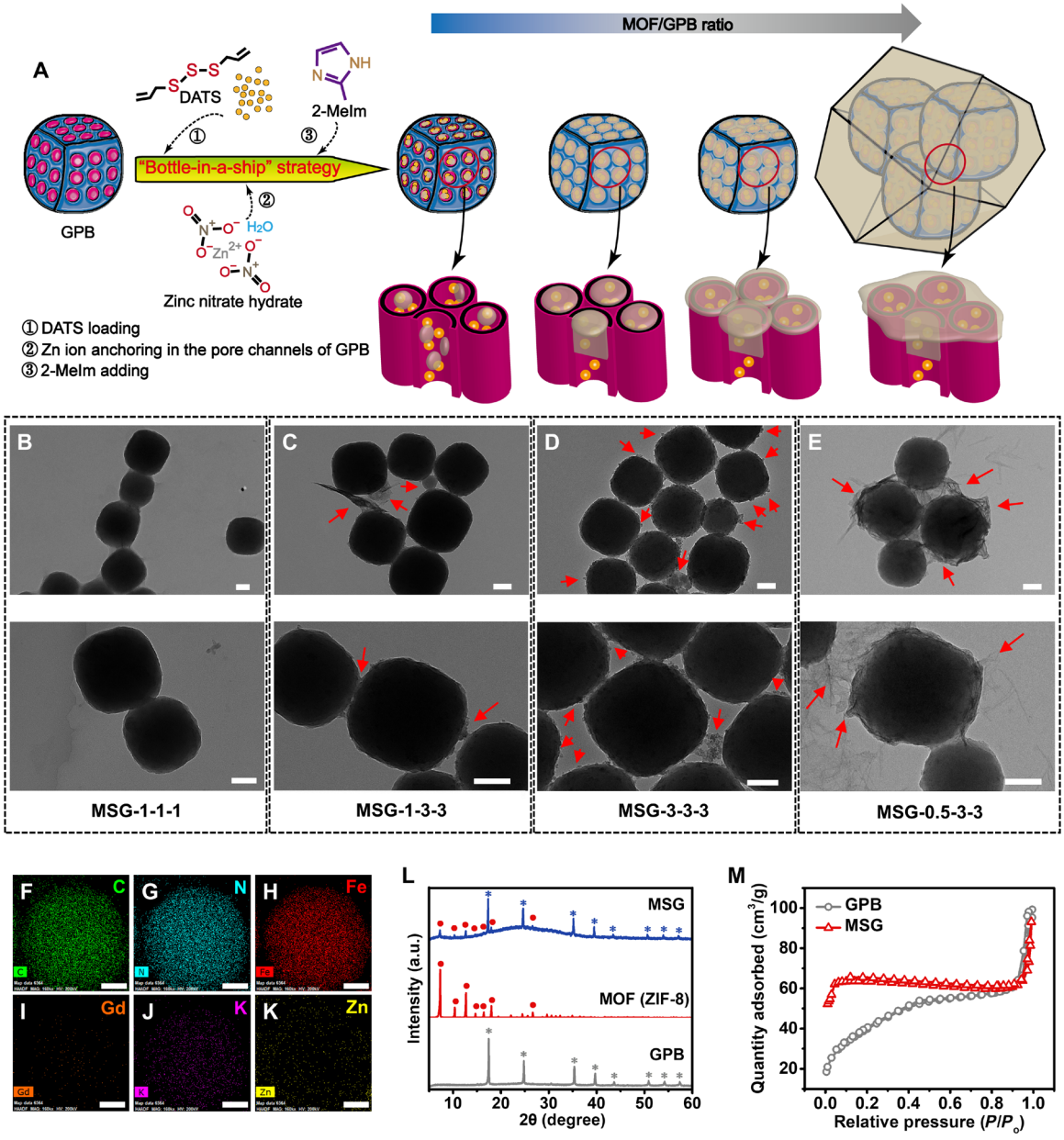

Fig. 4. Morphology and structure characterization of MSG. (**A**) Scheme of the construction of MSG heterostructure with different mass ratios of MOF/GPB. (**B** to **E**) TEM images of the MSG nanostructures with different mass ratios of MOF/GPB. Scale bars, 100 nm. The *x*, *y*, and *z* in MSG-*x*-*y*-*z* represent the mass ratio of GPB-III, $Zn(NO_3)_2$, and 2-MeIm. (**F** to **K**) HAADF-STEM mapping of MSG with the elements of C, N, Fe, Gd, K, and Zn. Scale bars, 80 nm. (**L**) XRD patterns of GPB, MOF (ZIF-8), and MSG. (**M**) N_2 adsorption-desorption isotherms of GPB and MSG.

both MSG-1-0.5-0.5 (Zn/Fe mass ratio = 0.16) and MSG-3-1-1 (Zn/Fe mass ratio = 0.14) was lower than that of MSG-1-1-1 (Zn/Fe mass ratio = 0.40), further confirming the incomplete MOF sealing in MSG-1-0.5-0.5 and MSG-3-1-1 (fig. S11C). However, the reaction of exceedingly high concentration of $Zn(NO_3)_2$ and 2-MeIm with a minute amount of GPB resulted in the unwanted nucleation of MOF nanoparticles (Fig. 4, C and D, and fig. S12), and even MOF-coated aggregated GPB (Fig. 4E), as shown in the corresponding photographs of the synthesized MSG in DI water (figs. S13 and S14). Considering all the above relevant factors, we picked MSG-1-1-1 for further use as the nanocarrier.

Elemental mapping and x-ray energy-dispersive spectroscopy spectrum showed the uniform distribution of additional Zn ions on the surface of GPB, which provided additional support for the successful sealing of MOF in the channels of GPB (Fig. 4, F to K, and fig. S15). The zeta potential of MSG was still negative (fig. S16), and it exhibited a narrow hydrolyzed particle size distribution (PDI = 0.117; fig. S17), indicating its efficiency in water dispersity. The XRD pattern (Fig. 4L) of MSG showed the characteristic peaks of MOF (ZIF-8) at around 7.32°, 10.37°, 12.71°, 14.69°, 16.44°, and 26.66° (marked by sphere signs) as well as GPB at around 17.46°, 24.80°, 35.35°, 39.70°, 43.65°, 50.86°, 54.21°, and 57.37° (marked by stellate signs). The high-resolution x-ray photoelectron spectroscopy (XPS) spectra (fig. S18) also revealed the binding energies of Fe 2p, Gd 4d, and Zn 2p in MSG, all of which further confirmed the MSG heterostructure composed of GPB and MOF. According to the Brunauer-Emmett-Teller (BET) results, small molecules can be loaded into the pore channels of GPB (Fig. 4M and fig. S10A). The decreased pore volume of MSG suggested the successful MOF sealing in the pore channels of GPB (fig. S10B). In addition, the photothermal conversion tests also demonstrated that the MOF sealing had negligible influence on the photothermal conversion of GPB (fig. S19), so MSG could be used for photothermal therapeutic application as well as controlled drug delivery/release.

DATS release and H_2S generation

DATS, a typical H_2S prodrug, was entrapped in the pore channels of GPB (denoted as DATS-GPB). Subsequently, MOF was synthesized to seal the pore channels of DATS-GPB (denoted as MSDG) to prevent DATS from robust release (Fig. 4M). The characterization of DATS revealed that its encapsulation efficiency was 22.00%, and its loading capacity was 18.93% (fig. S20). Because of the apt protonation of imidazolate ligands in MOF, metal-ligand coordination bonds are unsteady in humid and acidic environments (*44*, *45*). The MOF was found to exhibit acidity-activated degradation based on the release of Zn ions from MSDG at different pH values. The robust release of Zn ions from MSDG was observed in acidic solution (pH 5.0, 6.0), signifying the acidity-triggered degradation of MOF (Fig. 5, A and B). In contrast, there was much slower Zn ion release at pH 7.4 (Fig. 5C), demonstrating negligible MOF degradation at a neutral solution that effectively prevented drug leakage in the neutral microenvironment of physiological pH (Fig. 5D). Moreover, the Fe/Gd release patterns showed no visible difference between the acidic and neutral environments (Fig. 5, A to C), suggesting the high stability of GPB with negligible degradation irrespective of the changes in surrounding pH.

The release pattern of DATS from MSDG exhibited a trend very similar to the degradation pattern of MOF (Fig. 5E). Ultraviolet-visible (UV-Vis) spectra were measured to detect the released DATS in the presence of buffers with various pH (fig. S21). As expected, MSDG showed a very slow DATS release pattern in a neutral environment but a robust and rapid DATS release pattern in an acidic environment (Fig. 5E and fig. S22). In addition, we investigated the influence of NIR light on the release of DATS (fig. S23). The NIR laser irradiation could not affect the DATS release significantly. The main mechanism of DATS release is ascribed to the acidity-triggered MOF degradation. However, the heat arising from the NIR laser irradiation cannot induce the MOF degradation due to the thermal stability of MOF (ZIF-8) (*46*). To further identify the key role of MOF sealing in protecting DATS from spontaneous release, large-sized core/shell-structured GPB@MOF particles without MOF sealing were prepared (fig. S24). This structure hardly prevented DATS release in both neutral and acidic environments (fig. S25) because of the insufficient deposition of MOF inside the pore channels of GPB. It has been reported that DATS specifically responds to the thiol stimuli (e.g., GSH) to generate H_2S via thiol-disulfide exchange and subsequent allyl perthiol reduction (*35*, *36*). The generated H_2S was measured using the typical methylene blue method (*47*), according to the standard curves (figs. S26 and S27). We also detected invisible H_2S release from MSDG without the presence of GSH irrespective of pH. Only the acidic environment with GSH could induce a robust and sustained H_2S release from MSDG, which was attributed to the acidity-activated MOF degradation resulting in the exposure of DATS to GSH (Fig. 5F). Fortunately, there exists an acidic and GSH-overexpressed microenvironment in biofilms (*12*, *14*–*17*), so MSDG is expected to achieve BME-responsive H_2S release for precise biofilm-specific therapy. It is noteworthy that bacillithiol, as the functional analog of GSH in *S. aureus* (*48*), can also trigger the splitting of DATS to generate H_2S gas (*35*, *36*).

In vitro antibiofilm activity assay

To explore the antibiofilm activity of MSDG in vitro, we selected *E. coli* and MRSA biofilms as the model candidates with different treatments, namely, Control (untreated), NIR, MSG, MSDG (H_2S gas), MSG + NIR, and MSDG (H_2S gas) + NIR groups. The concentrations of both MSG and MSDG in the groups of MSG, MSDG, MSG + NIR, and MSDG + NIR for in vitro antibiofilm treatment (Fig. 6) are 30 μg/ml. Around 10 min before NIR irradiation, MSG or MSDG solutions were applied to biofilms. Hyperthermia was applied in the MSG + NIR and MSDG + NIR groups for 10 min and monitored by an infrared thermal imaging camera to maintain a temperature of approximately 50°C (fig. S28). The released H_2S gas in the inner biofilm was detected by Washington state probe-1 (WSP-1), as bright green fluorescence (fig. S29). Through crystal violet staining, the biofilm in groups treated with Control, NIR, MSG, and MSDG remained mostly viable and structurally intact, indicating no significant antibiofilm activity (Fig. 6A). Instead, hyperthermia disrupted the tight biofilm (lighter purple) causing significant biomass loss in the MSDG + NIR group (Fig. 6, B and C). The number of colony-forming units (CFU) demonstrated intact bacterial survival in the MSG and MSDG groups, indicating that they failed to exert any antibiofilm activity via MSG, DATS, or H_2S gas in both *E. coli* and MRSA bacterial biofilms (Fig. 6D). However, the MSG + NIR and MSDG + NIR groups with hyperthermia presented remarkable antibiofilm effects. As shown in Fig. 6 (E and F), the MSDG + NIR group showed stronger biofilm inhibition ability than the other groups. Three-dimensional reconstructions of fluorescence-labeled *E. coli* and MRSA biofilms stained with Syto9 (green, live bacteria) were performed to determine the changes in biofilm structure to evaluate

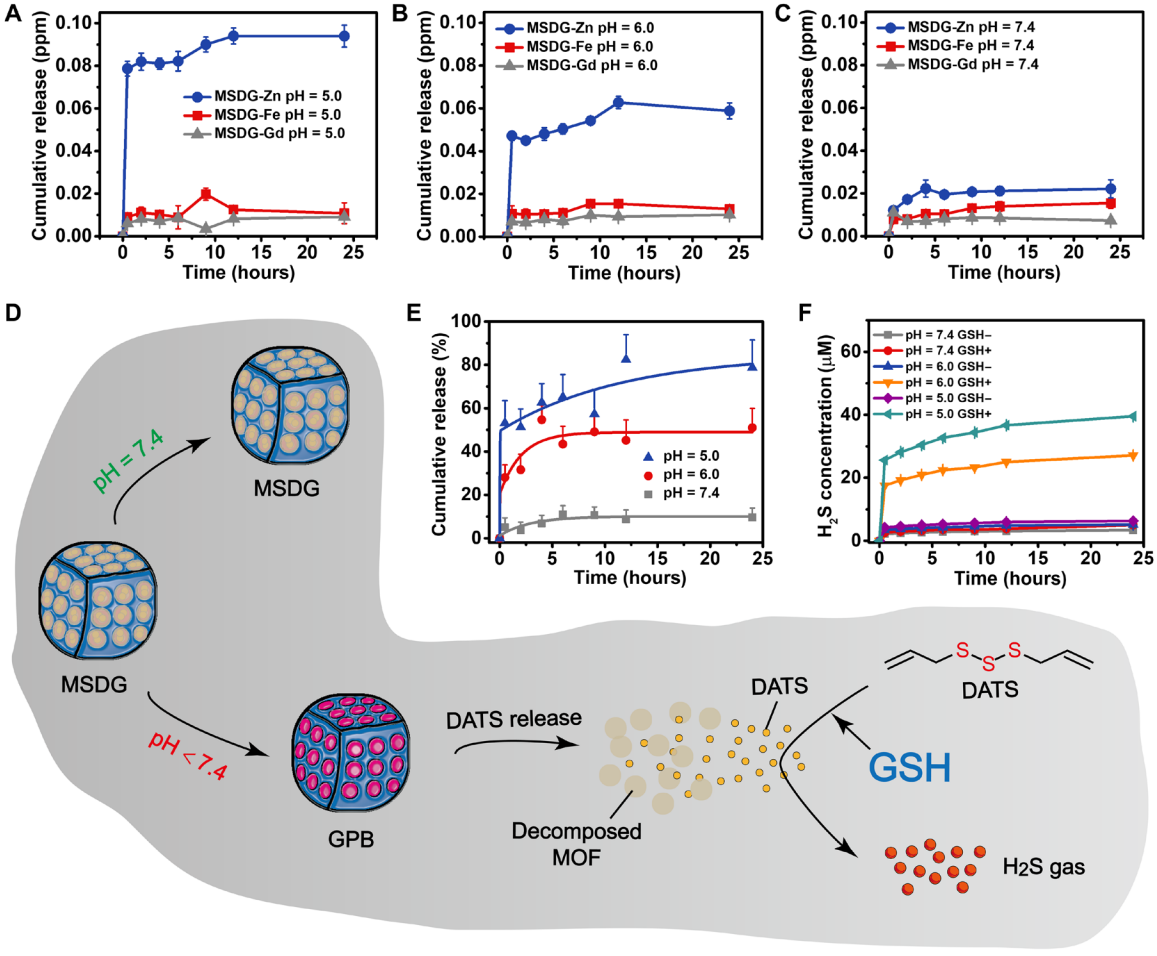

Fig. 5. H_2S release patterns of MSDG. (**A** to **C**) Release patterns of Zn, Fe, and Gd ions from MSDG at (A) pH 5.0, (B) pH 6.0, and (C) pH 7.4. $n = 3$, means ± SD. ppm, parts per million. (**D**) Scheme of DATS release and H_2S generation from MSDG under different pH values. (**E**) Release patterns of DATS from MSDG at different pH values. $n = 3$, means ± SD. (**F**) Release patterns of H_2S from MSDG with or without 2 mM GSH incubation at different pH values. $n = 3$, means ± SD.

the effect of various treatments. For the Control, NIR, MSG, and MSDG groups, bright green fluorescence was observed, indicating intact bacterial biofilms (Fig. 6G). Broken bacterial biofilms with scattered green fluorescence were observed in the MSG + NIR and MSDG + NIR groups. The corresponding quantitative results of these groups also depicted significant biofilm destruction with declining relative fluorescence intensity (fig. S30). Furthermore, high bacterial density and unperturbed bacterial morphology were observed in the Control, NIR, MSG, and MSDG groups with a scanning electron microscope (SEM) (Fig. 6H). In contrast, the majority of *E. coli* and MRSA bacteria inside biofilm became shriveled, distorted, or even wholly lysed after incubation with MSG and MSDG upon NIR laser irradiation, validating their efficiency in biofilm elimination. Therefore, we found that single gas therapy using H_2S (MSDG group) or hyperthermia (MSG + NIR group) had limited antibiofilm activity. However, the synergistic combination of gas therapy and hyperthermia (MSDG + NIR group) efficiently eliminates biofilms.

Mechanism of H_2S-sensitized hyperthermia for biofilm elimination

As a bioadhesive component for bacterial adhesion and biofilm stabilization, eDNA is responsible for efficiently integrating the adjacent EPS and bacteria into the intact biofilm (*23*, *49*, *50*). Because of the similarity between the genomic DNA (gDNA) of bacteria and the eDNA (*50*, *51*), the gDNA was extracted and dispersed in aqueous solution for different treatments. According to the agarose gel electrophoresis result (Fig. 7A), H_2S gas released from MSDG could break the gDNA, confirming the H_2S-induced eDNA damage. To investigate the potential antibiofilm mechanism via H_2S-sensitized hyperthermia, the eDNA levels in each group were measured using the green fluorescence analysis (Fig. 7B and fig. S31). Both MSDG and MSDG + NIR groups effectively releasing H_2S gas exhibited low eDNA levels in the biofilms, which was consistent with the results obtained by eDNA content assay, regardless of the bacterial species (Fig. 7, C and D). Although hyperthermia reduced eDNA levels in the biofilms, the combination of gas therapy and hyperthermia had the best eDNA damaging capability. In conclusion, H_2S gas released from MSDG is a DNA-damaging mutagen that causes breaks in eDNA and facilitates the collapse of the solid biofilm.

After the destruction of the biofilm structure by H_2S gas, NIR laser–activated hyperthermia continued to kill the bacteria from the fragmented biofilm. On that basis, o-nitrophenyl-β-$_D$-galactopyranoside (ONPG) can penetrate into membrane-damaged cells (*52*, *53*). The ONPG hydrolysis assay was used to evaluate the membrane

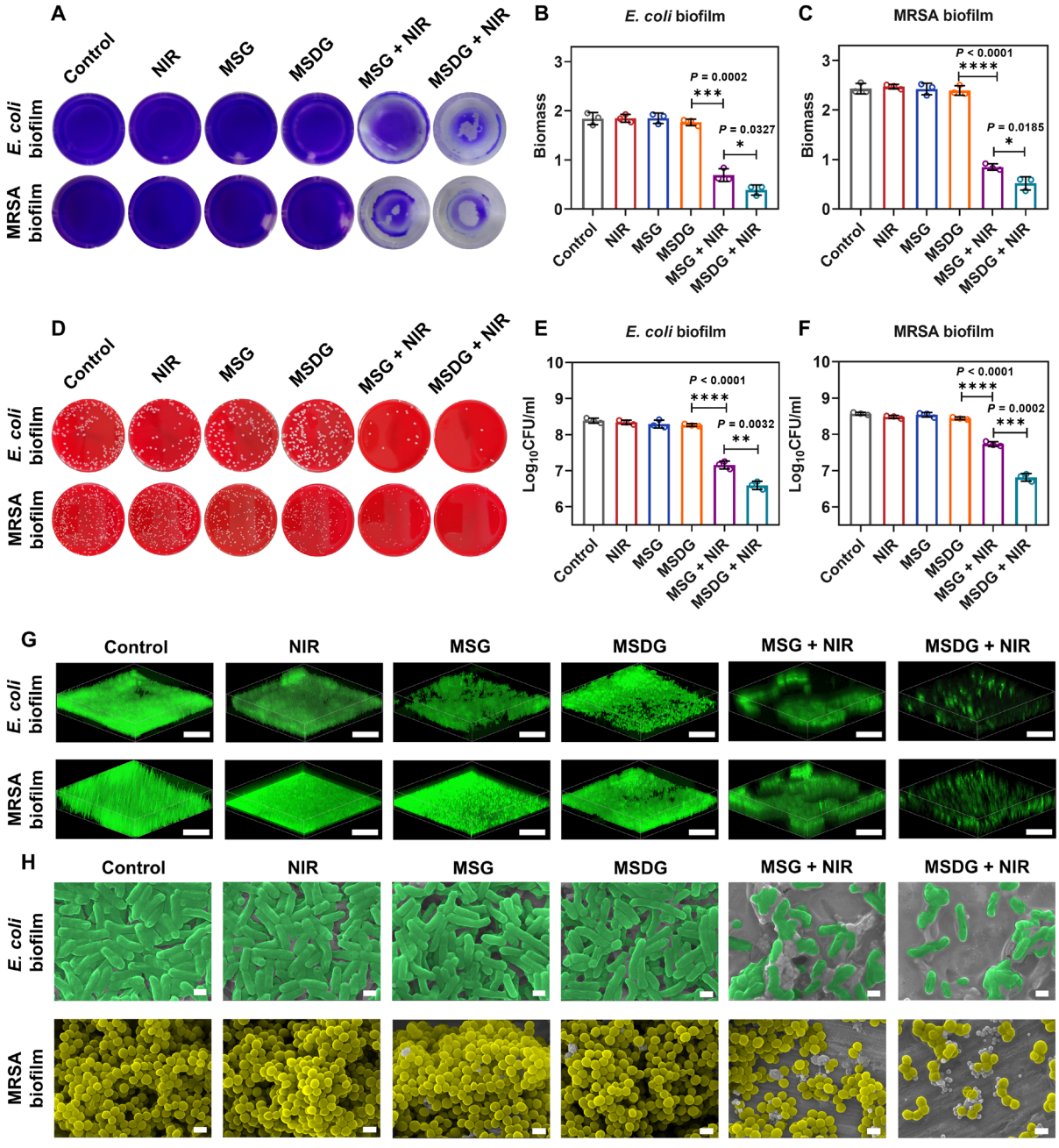

Fig. 6. In vitro evaluation of the antibiofilm activity. (**A**) Macroscopic *E. coli* and MRSA biofilm images of Control-, NIR-, MSG-, MSDG-, MSG + NIR–, and MSDG + NIR–treated groups with crystal violet staining. Biofilm biomass of (**B**) *E. coli* and (**C**) MRSA biofilms after various treatments. (**D**) Typical photos of disrupted bacterial colonies from *E. coli* and MRSA biofilms in Control-, NIR-, MSG-, MSDG-, MSG + NIR–, and MSDG + NIR–treated groups. Number of CFU of (**E**) *E. coli* and (**F**) MRSA in six different treatment groups determined by SPM. (**G**) Three-dimensional reconstructions of the fluorescence-labeled *E. coli* and MRSA biofilms stained with Syto9 (indicating live bacteria). Scale bars, 30 μm. (**H**) High-resolution SEM images of *E. coli* and MRSA biofilms treated with Control, NIR, MSG, MSDG, MSG + NIR, and MSDG + NIR. Scale bars, 1 μm. $n = 3$; means ± SD; $^{*}P < 0.05$, $^{**}P < 0.01$, $^{***}P < 0.001$, and $^{****}P < 0.0001$ using Student's *t* tests.

permeability of *E. coli* and MRSA bacteria detached from the biofilm (Fig. 7, E and F). In the Control, NIR, MSG, and MSDG groups, the bacteria displayed an intact cell membrane structure without cytoplasm leakage and prevented the entry of ONPG. The MSG + NIR group with hyperthermia alone exhibited improved bacterial membrane destructive capability than the MSDG group with H_2S gas alone. Moreover, the MSDG + NIR group showed the stronger destructive ability on the bacterial membrane, implying the synergistic effect of H_2S gas combined with hyperthermia. Likewise, flow scatter diagrams revealed augmented propidium iodide (PI)–positive rates, which signified bacterial death, indicating an efficient bactericidal capacity (Fig. 7G and fig. S32). The schematic illustration of Fig. 7H and fig. S33 revealed the biofilm elimination mechanism of H_2S-sensitized hyperthermia, including eDNA damage and bacterial killing.

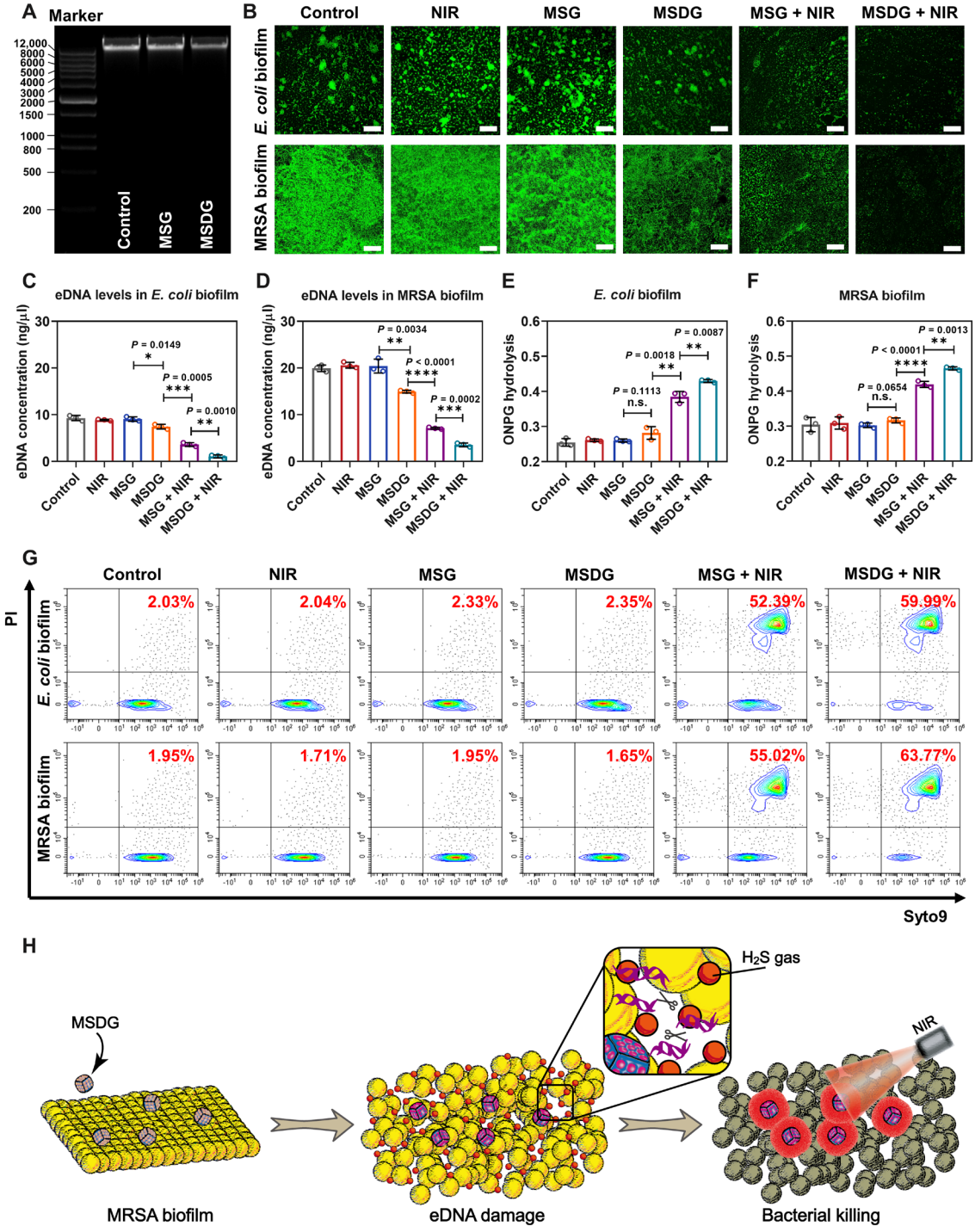

Fig. 7. Mechanism of H_2S-sensitized hyperthermia for biofilm elimination. (**A**) Agarose gel electrophoresis result of bacterial gDNA treated by MSG and MSDG. (**B**) SYTOX staining of eDNA in *E. coli* and MRSA biofilms. Scale bars, 200 μm. eDNA levels in (**C**) *E. coli* and (**D**) MRSA biofilms. Membrane permeability evaluation by ONPG hydrolysis assay of (**E**) *E. coli* and (**F**) MRSA detached from the biofilms after various treatments. (**G**) Flow scatter diagrams of PI and Syto9 costaining of *E. coli* and MRSA detached from the biofilms after various treatments. (**H**) Schematic illustration of the mechanism of biofilm elimination by H_2S-sensitized hyperthermia. $n = 3$; means ± SD; n.s., no significant; *$P < 0.05$, **$P < 0.01$, ***$P < 0.001$, and ****$P < 0.0001$ using Student's *t* tests.

In vivo antibiofilm activity

Encouraged by the remarkable biofilm elimination ability of MSDG in vitro, we further investigated the antibiofilm effects in vivo using a mouse implant–related infection model. The comprehensive procedure of the antibiofilm treatment in vivo is depicted in Fig. 8A. Briefly, 3 days before the insertion of implants infested with biofilm, MRSA suspension (10^7 CFU/ml) was dropped onto polyether-ether-ketone (PEEK) washers to prepare MRSA biofilms. Two days after

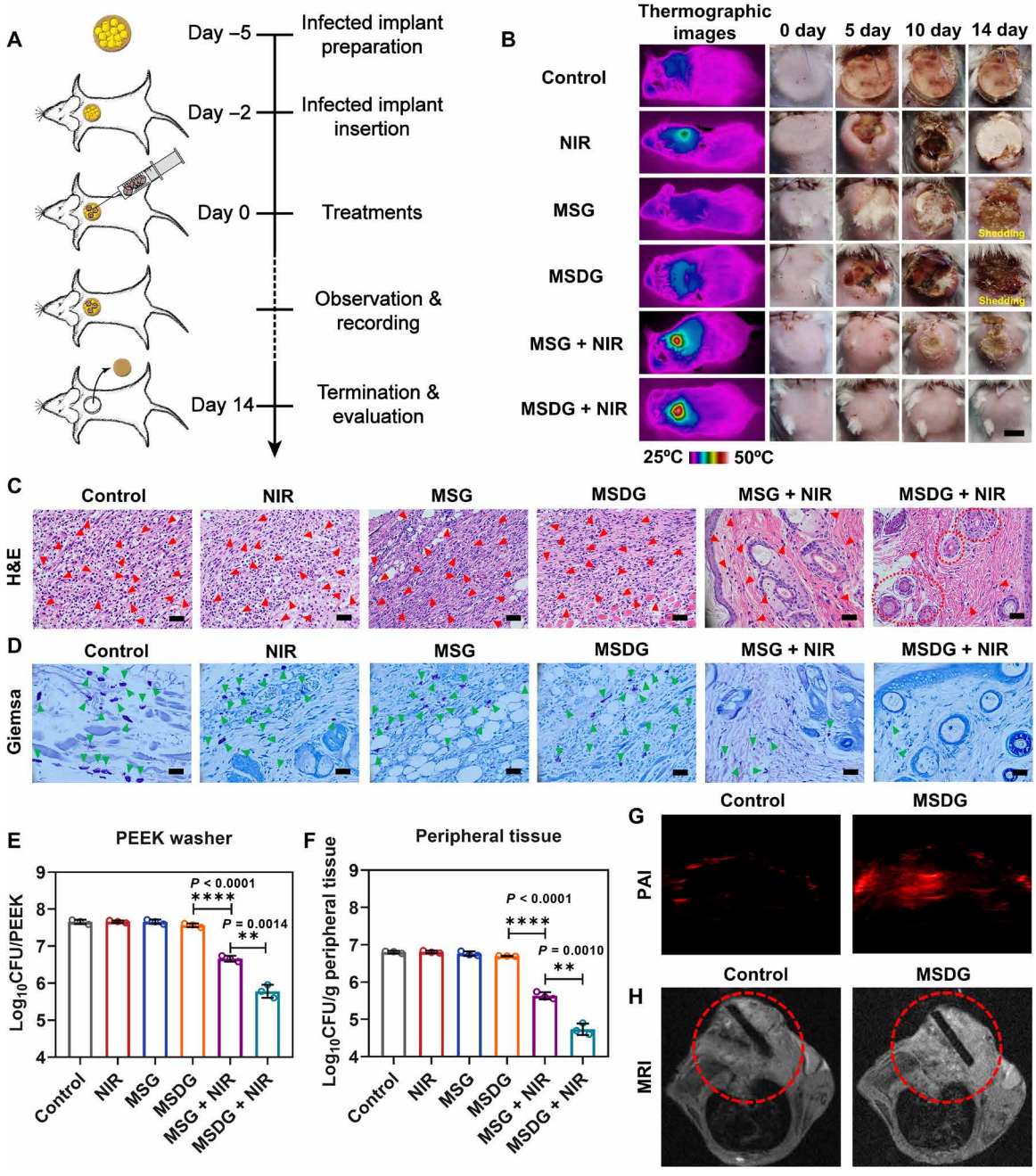

Fig. 8. In vivo evaluation of antibiofilm activity using the mouse implant–related infection model. (**A**) Schematic diagram of the in vitro treatment procedure for the antibiofilm assay. (**B**) Macroscopic photos of the skin tissue in six different treatments with thermographic images of 10 min. Scale bar, 0.5 cm. Histomorphological analyses via (**C**) H&E and (**D**) Giemsa staining of the peripheral tissue after various treatments. Scale bars, 50 μm. Quantitative measurements of residual biofilm on (**E**) the surface of the implants and (**F**) residual bacteria in the peripheral tissues after treatment. (**G**) PAI images at 808 nm before and after MSDG injection at the site of abscess. (**H**) MRI images of the site of abscess before and after the injection with MSDG. $n = 3$; means ± SD; $^{**}P < 0.01$ and $^{****}P < 0.0001$ using Student's t tests.

implant insertion (fig. S34), the mice were randomly divided into six groups according to the separate treatments: Control, NIR, MSG, MSDG (H_2S gas), MSG + NIR, and MSDG (H_2S gas) + NIR. Then, 200 μl of MSG and MSDG solutions (30 μg/ml) was applied in different treatments. There was an incubation time of about 10 min after injection and before NIR laser irradiation. The temperature variation trend of MSG + NIR and MSDG + NIR in vivo was monitored using an infrared thermal imaging camera (Fig. 8B, first column). The temperature of the sites of injected abscesses rapidly rose from 32.5° to 47.4°C upon NIR laser irradiation (808 nm, 1.0 W/cm^2) in 200 s for the MSDG + NIR group. However, only minute temperature fluctuation (32.8° to 38.1°C) was observed in the NIR group with the same power intensity of NIR laser irradiation (fig. S35). H_2S release in vivo was detected by H_2S probe (WSP-5) on the in vivo imaging system (IVIS). We could observe the bright fluorescence at the infectious sites, which testified the in vivo H_2S release (fig. S36). During

the 14-day treatment period, macroscopic photographs of skin tissue with subcutaneous implant were shown in Fig. 8B. Swelling, suppuration, and even implant exposure/shedding were observed in the Control, NIR, MSG, and MSDG groups, implying a biofilm-induced inflammatory response at the abscess sites (Fig. 8B, first, second, third, and fourth rows). Negligible swelling of the scabby skin tissue was found in the MSG + NIR group, indicating effective antibiofilm activity via hyperthermia alone (Fig. 8B, fifth row). There was no swelling, purulence, or wound fester observed in the MSDG + NIR group, suggesting that the best antibiofilm activity could be obtained through H_2S-sensitized hyperthermia (Fig. 8B, sixth row).

Furthermore, the peripheral tissues of the infectious sites were harvested for histomorphological and quantitative analyses on day 14 after implantation. Hematoxylin and eosin (H&E) staining photographs showed abundant neutrophil infiltration (red arrows) in the Control, NIR, MSG, and MSDG groups, indicating the infection-induced inflammatory response. However, the inflammation was well controlled in the MSDG + NIR group due to H_2S-sentisized hyperthermia (Fig. 8C and fig. S37A). Giemsa staining proved the bacterial infiltration (green arrows) in the Control, NIR, MSG, and MSDG groups. In contrast, MSDG + NIR suppressed bacterial infiltration into peripheral tissue (Fig. 8D and fig. S37B). The quantitative results of bacterial residues on PEEK washers and bacterial infiltration in the peripheral tissues after various treatments were also evaluated by estimating the number of CFU. As expected, the number of bacterial colonies in the MSDG + NIR group was considerably lower than that in the other five groups, which further substantiated the prominent antibiofilm activity of H_2S-sensitized hyperthermia (Fig. 8, E and F). The SEM images also showed that there were the fewest residual bacteria on the PEEK washer in the MSDG + NIR group (fig. S38). In contrast, many biofilms and dense clustered bacteria could still be observed in the other groups. In addition, MSDG could be used as an MRI/PAI contrast enhancement agent, which might be beneficial for diagnostic applications in vivo (Fig. 8, G and H).

In vitro immunomodulatory function

Sectional hair follicles and angiogenesis in the MSDG + NIR group prompted our research interest in the tissue remodeling ability of MSDG (H_2S gas) after eliminating biofilms (Fig. 8C and fig. S39, red circles). Highly plastic macrophages are crucial for homeostasis, host defense, and tissue remodeling (*54*). Accordingly, macrophages were coincubated with MSG and MSDG. The released H_2S in the MSDG group was detected using a WSP-1 probe (fig. S40). The flow scatter diagrams showed amplified M2 polarization in the MSDG group with the significant increase in CD206-positive cells from 11.67 to 29.24% (Fig. 9A and fig. S41A). However, the number of CD86-positive cells was unperturbed (fig. S41B). In the MSG group, there was no significant change in the number of CD206-positive cells, indicating that MSG could not induce the M2 macrophage polarization. The 4′,6-diamidino-2-phenylindole (DAPI)/ fluorescein isothiocyanate (FITC) staining of macrophages presented the transformation of macrophage status from M0 to M2, with morphologies evolved from cluster-like to elongated cellular shapes (Fig. 9B). Furthermore, the immunofluorescence staining of CD206 (M2 marker) validated the MSDG-mediated M2 macrophage polarization from M0 macrophage (fig. S42). Real-time quantitative polymerase chain reaction (RT-qPCR) results revealed distinct increase in expression of M2 marker genes, including arginase-1 (Arg-1) and CD206. However, there was no remarkable change in the expression of the M1 marker gene, inducible nitric oxide synthase (iNOS) (Fig. 9, C to E). Corresponding to this, tissue regeneration–related gene expression of vascular endothelial growth factor (VEGF) was substantially up-regulated in the MSDG group (Fig. 9F). Meanwhile, enzyme-linked immunosorbent assay (ELISA) results on macrophages after MSDG treatment depicted a clear secretion-promoting effect of anti-inflammatory cytokine [interleukin-10 (IL-10)], but the expression level of pro-inflammatory cytokine (IL-1β) was unaltered (fig. S43). Although there are some reports about H_2S-induced M2 macrophage polarization (*20*, *31*), the corresponding mechanism needs to be further explored. Notably, H_2S-mediated adenosine monophosphate–activated protein kinase (AMPK) activation can promote the M2 polarization of microglia (*55*, *56*). The activation of AMPK can also promote M2 macrophage polarization (*57*, *58*). The similarity between microglia and macrophage inspires us to investigate the effect of H_2S gas on AMPK singling pathway activation in M2 macrophage polarization (fig. S44). The up-regulated phosphorylated AMPK (pAMPK) expression was observed in the MSDG group rather than in the groups of Control and MSDG + AMPK inhibitor (fig. S44, A and B). Moreover, the expression of Arg-1 and IL-10 was obviously decreased due to the block of AMPK signaling, further confirming H_2S-mediated AMPK singling pathway activation in M2 macrophage polarization (fig. S44C). On the basis of these results, it can be concluded that H_2S derived from MSDG exerted immunomodulatory effects on macrophage polarization facilitating the transformation toward the M2 phenotype.

In vitro immunomodulatory cell migration and angiogenesis

Subsequently, the immunomodulatory effects for the promotion of cell migration and angiogenesis by MSDG (H_2S gas) were investigated using macrophage-conditioned media in vitro. The transwell migration assay depicted that MSDG significantly stimulated the mobility of human umbilical vein fusion cells (EA.hy 926) compared to the other groups (Fig. 9G). Similar quantitative measurements were used to determine the number of cells that migrated through the polycarbonate filters (Fig. 9H). Meanwhile, the scratch assay also revealed efficient cell migration ability with a shrunken scratch area in the MSDG group (Fig. 9, I and J). In the tube formation test, EA.hy 926 cells exhibited an ascending number of junctions and tubes in the MSDG coincubated macrophage-conditioned media, indicating increased vascular formation (Fig. 9, K and L). These results demonstrated that the M2 macrophages could secrete abundant regeneration-related cytokines to promote cell migration and angiogenesis of endothelial cells. Therefore, MSDG with the generation of H_2S gas presented immense potential for promoting tissue remodeling.

In vivo immunomodulatory tissue remodeling

After successful evaluation of the antibiofilm activity in vivo, MSDG (H_2S gas)–mediated improvement of immune microenvironment and tissue remodeling was investigated next. Biofilm-induced inflammatory responses critically suppressed the tissue remodeling due to the production of high levels of pro-inflammatory cytokines [e.g., tumor necrosis factor–α (TNF-α) and IL-6] in the Control group (Fig. 10A and fig. S45). Immunofluorescent costaining of TNF-α/IL-6 showed remarkably alleviated levels of IL-6 and TNF-α in the MSDG + NIR group due to the anti-inflammatory effects, M2 macrophage polarization, and effective antibiofilm activity (*30*, *31*, *59*).

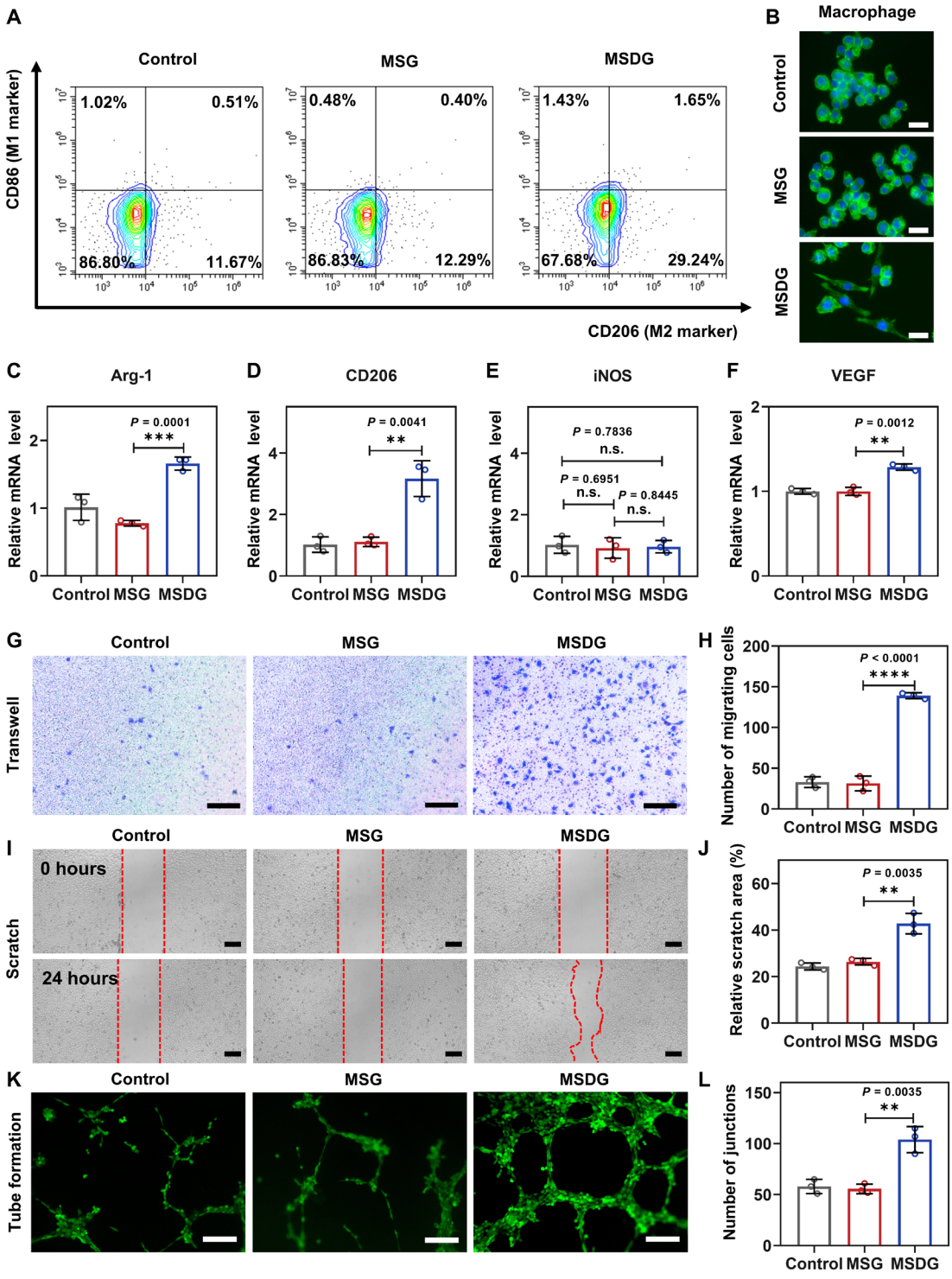

Fig. 9. In vitro evaluation of immunomodulatory functions. (**A**) Flow scatter diagrams of CD86 (M1 marker) and CD206 (M2 marker) expression after different treatments with (**B**) corresponding macrophage staining using 4′,6-diamidino-2-phenylindole (DAPI; nucleus) and fluorescein isothiocyanate (FITC; cytoskeleton). Scale bars, 25 μm. RT-qPCRs results of (**C**) Arg-1, (**D**) CD206, (**E**) iNOS, and (**F**) VEGF in RAW264.7. (**G**) Transwell migration assay for EA.hy 926 in different groups with (**H**) quantitative analysis of the number of migrating cells. Scale bars, 200 μm. (**I**) Scratch assay of EA.hy 926 cells cultured in macrophage-conditioned media for 0 and 24 hours with (**J**) quantitative analysis of relative scratch area. Scale bars, 100 μm. (**K**) Vascular tube formation of EA.hy 926 cells cultured in various macrophage-conditioned media on Matrigel for 6 hours with (**L**) quantitative analysis of the number of junctions. Scale bars, 200 μm. $n = 3$; means ± SD; $^{**}P < 0.01$, $^{***}P < 0.001$, and $^{****}P < 0.0001$ using Student's t tests.

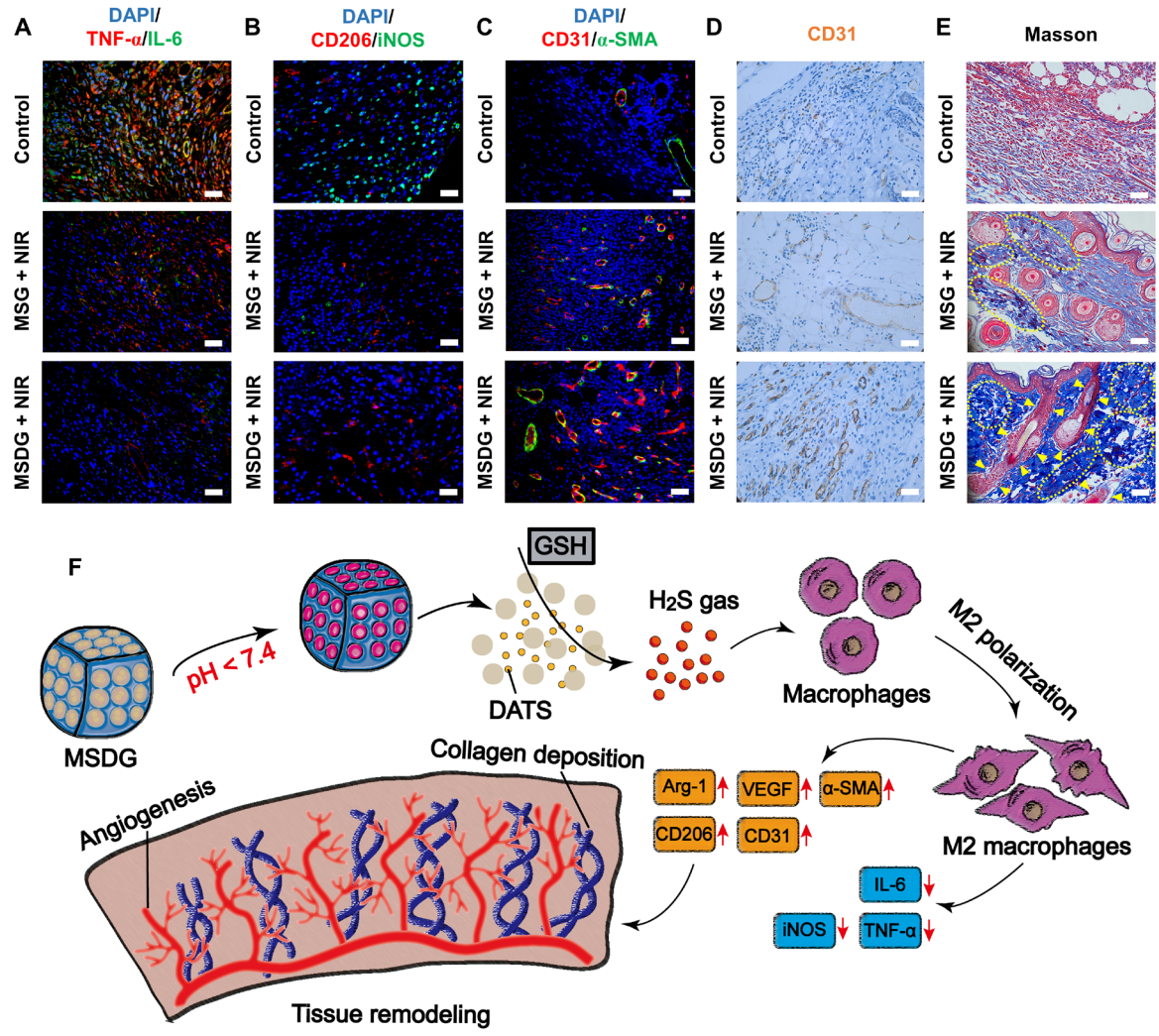

Fig. 10. In vivo evaluation of immunomodulatory tissue remodeling. Immunofluorescent costaining of (**A**) TNF-α/IL-6, (**B**) CD206/iNOS, and (**C**) CD31/α-SMA. Scale bars, 50 μm. (**D**) Immunohistochemical staining of CD31. Scale bars, 50 μm. (**E**) Histomorphological analysis via Masson's trichrome staining. Scale bars, 50 μm. (**F**) Schematic illustration of MSDG-mediated improvement of immune microenvironment and tissue remodeling.

Apparently, compared with the MSG + NIR group, the MSDG + NIR group showed much more positive staining of CD206 (red, M2 macrophages), suggesting the up-regulated number of M2 macrophages (Fig. 10B and fig. S46). Inevitably, biofilm-induced M1 polarization was observed in the Control group, exhibiting up-regulated iNOS (green, M1 macrophages) (*60*). H_2S-sensitized hyperthermia could eliminate most biofilms. H_2S-mediated M2 macrophage polarization could promote the secretion of regeneration-related cytokines to accelerate tissue remodeling. Therefore, the angiogenesis and vessel maturation were manifested in the MSDG + NIR group, with the highest expression of α-smooth muscle actin (α-SMA) (green, myofibroblast) and CD31 (red, endotheliocyte marker) (Fig. 10C and fig. S47). Similarly, immunohistochemistry assay also demonstrated numerous lots of CD31-positive cells in the MSDG + NIR group rather than in the MSG + NIR group (Fig. 10D). Quantitative measurements of collagen deposition revealed extensive (yellow circles) and new blood vessel formation (yellow arrows) in the MSDG + NIR group rather than in the MSG + NIR group (Fig. 10E and figs. S48 and S49). Together, MSDG with the generation of H_2S could reverse infection-induced pro-inflammatory microenvironment and effectively promote tissue remodeling after successful biofilm elimination (Fig. 10F).

In vitro and in vivo evaluation of biosafety

To evaluate the biosafety of MSDG in vitro, the cytotoxic effect of MSDG was assessed by measuring cell viability using CCK-8 (cell counting kit-8) assay. Accordingly, EA.hy 926 cells or RAW264.7 macrophages were incubated with MSDG at various concentrations. The relative cell viability remained above 97.50% in the presence of MSDG (30 μg/ml), indicating good biocompatibility (fig. S50). Therefore, the concentration of MSDG (30 μg/ml) was finalized as the optimal dose for all in vitro experiments. Although the NIR laser irradiation (808 nm, 1 W/cm^2) reduced the cell viabilities of EA.hy 926 and RAW264.7 cells when incubated with MSDG (30 μg/ml), the cell viabilities of both cells gradually increased after the NIR laser was removed (fig. S51). Notably, MSDG exhibited sufficient stability in various solutions including Dulbecco's modified Eagle's medium (DMEM), phosphate-buffered saline (PBS), serum, and water for at

least 4 days. The stability was estimated by recording the absorbance of MSDG in respective media at a wavelength of 808 nm (fig. S52). For in vivo toxicity assessment, the change in the average body weight of mice in different groups demonstrated negligible fluctuations, implying that the side effects of MSDG in animals were insignificant (fig. S53). Moreover, no detectable pathological changes or adverse effects were observed in the H&E staining of major organs, such as the heart, liver, spleen, lung, and kidney of the mice with MSDG treatment, further validating the high histocompatibility of MSDG in physiological context (fig. S54).

In summary, we introduce a convenient bottle-in-a-ship strategy for the controllable synthesis of BME-responsive MSDG for biofilm-specific H_2S-sensitized thermal eradication as well as immunomodulatory tissue remodeling. The sealing of MOF inside the pore channels of GPB can effectively prevent the premature drug leakage of DATS, but the acidic BME-responsive MOF degradation allows the release of DATS to react with the overexpressed GSH for considerable H_2S generation in the biofilm. Subsequently, H_2S-induced eDNA damage disperses the tight biofilm and largely increase the sensitivity of biofilm to the hyperthermia arising from NIR laser–activated GPB, which gives rise to substantially improved bacterial killing effects for thorough biofilm elimination. The generated H_2S can promote the polarization of macrophages toward M2 phenotype for ameliorating the immune microenvironment. Under the stimulation of MSDG, M2 macrophages can secrete abundant regeneration-related cytokines to accelerate tissue remodeling in an implant-related infection model. Therefore, our proposed "H_2S-sensitized hyperthermia" bactericidal strategy and macrophage-associated immune regulation may establish an alternative nonantibiotic treatment for combating refractory implant–related infections.

MATERIALS AND METHODS

Materials

Potassium ferricyanide ($K_3[Fe(CN)_6]$), zinc nitrate [$Zn(NO_3)_2$], gadolinium nitrate [$Gd(NO_3)_3$], zinc acetate, sodium acetate, 2-MeIm, *N*,*N*-dimethyl-*p*-phenylenediamine dihydrochloride (DMPD), sodium sulfide (Na_2S), GSH, and PVP (K29-32) were purchased from Aladdin (China). Hydrochloride acid (36.0 to 38.0%) was purchased from Sinopharm Chemical Reagent Co. Ltd. (China). DATS was purchased from Yuanye (China). WSP-1 was purchased from Shanghai Maokang Biotechnology Co. Ltd. (China). PEEK platelets (10 mm × 10 mm × 1 mm) were purchased from Aosheng Materials Co. (China). All chemicals were used directly without further purification.

Preparation of PB with various sizes

Thirty-three milligrams of $K_3[Fe(CN)_6]$ was dissolved in 10 ml of aqueous HCl solution with varied concentrations (0.001, 0.01, 0.1, and 1.0 M). Next, aqueous PVP solution (0.36 g/ml) was added to the above mixed solution for 20 hours of magnetic stirring at 80°C. Then, the PB products were collected by centrifugation, washed three times with ethanol/water, and freeze-dried for further use.

Preparation of GPB with various Gd contents

Thirty-three milligrams of $K_3[Fe(CN)_6]$ was dissolved in 10 ml of aqueous HCl solution (0.1 M). Next, aqueous PVP solution (0.36 g/ml) with varied concentrations (25, 50, 100, and 200 mg/ml) of $Gd(NO_3)_3$ was added to the above mixed solution for 20 hours of magnetic stirring at 80°C. Then, GPB products were collected by centrifugation, washed three times with ethanol/water, and freeze-dried for further use.

Preparation of DATS-GPB

DATS and GPB were mixed in 10 ml of dimethyl sulfoxide (DMSO) with different mass ratios (DATS:GPB = 10:10, 5:10, and 2:10). Subsequently, the mixed solution was stirred at room temperature for 12 hours to allow sufficient loading of DATS into GPB. The DATS-loaded GPB (DATS-GPB) products were collected by centrifugation and washed with DMSO several times.

Preparation of MSDG

Eighty microliters of $Zn(NO_3)_2$ solution (×0.25, ×0.5, ×1.0, ×2.0, ×3.0) was added into 400 μl of DATS-GPB suspension (×0.5, ×1.0, ×3.0) in ice bath, followed by quick dropping of 800 μl of 2-MeIm solution (×0.25, ×0.5, ×1.0, ×2.0, ×3.0). The final MSDG products were centrifuged, washed with water, and freeze-dried for further use.

Characterizations

XRD patterns were taken on an X'Pert MPD x-ray diffractometer with Cu Kα radiation (λ = 1.5405 Å). XPS spectra were obtained with a Thermo ESCALAB 250Xi x-ray photoelectron spectrometer (Al Ka *hν* = 1486.6 eV, power = 150 W, x-ray beam spot = 500 μm, fixed transmission energy of energy analyzer = 30 eV). UV-Vis spectra were measured with a HITACH UH 5300 UV-Vis spectrophotometer. Transmission electron microscope (TEM) images were obtained with a JEM-2011 microscope. High-angle annular dark field–scanning transmission election microscope (HAADF-STEM) and element mapping images were obtained with a FEI Talos F200X microscope. Chemical compositions of materials were probed by Nicolet 8700 FTIR spectroscopy. Hydrolyzed particle size distribution and zeta potential were measured with Nano-ZS90 Malvern Zetasizer. Element concentrations were quantified with VG ELEMENTAL PlasmaQuad 3 [inductively coupled plasma mass spectrometry (ICP-MS)]. N_2 adsorption-desorption isotherm and pore size distribution were tested on a surface area and with a porosity analyzer (Tristar II 3020M).

Photothermal test

PB, GPB, and MSG were irradiated by an 808-nm laser (ADR-1860) with varied power densities (0.5, 1.0, 1.25, and 1.5 W/cm^2) for 5 min. An infrared thermal imaging camera (FOTRIC 220s, FOTRIC Thermal Intelligence Co., China) was adopted to record the real-time temperature of the three samples with varied concentrations (0.01, 0.05, 0.1, 0.25, and 0.5 mg/ml). The heating and cooling curves of samples (1.0 mg/ml) were obtained upon 808-nm laser irradiation (1.0 W/cm^2). PTCE (η) was calculated on the basis of the following formula

$$\eta = \frac{hS(T_{max} - T_{surr}) - Q_0}{I(1 - 10^{-A_{808}})} \quad (1)$$

$$\tau_s = \frac{m_d C_d}{hS} \quad (2)$$

$$Q_0 = hS(T_{max,water} - T_{surr}) \quad (3)$$

τ_s, as the characteristic thermal time constant, can be calculated from the linear regression curve in the cooling curve. m_d and C_d represent the mass of the solution and the heat capacity, respectively.

hS can be calculated from Eq. 2. Q_0 can be calculated from Eq. 3 with steady-state maximum temperature of water ($T_{max, water}$) and ambient room temperature (T_{surr}). *I* and A_{808} represent the laser power (0.785 W) and the absorbance of samples at 808 nm, respectively. Then, PTCE (η) can be calculated from Eq. 1.

In vitro T_1-weighted MRI and PAI of GPB

Varied concentrations of GPB solution were used for T_1 relaxivity measurement on a 7.0-T Bruker BioSpec small-animal MRI system. Besides, GPB solution with varied concentrations was set in capillary tubes for PAI on a Vevo LAZR PAI system.

DATS release from MSDG

Equal amounts of MSDG (1 mg/ml, 1 ml) in dialysis membrane bags (M_w = 10,000) were incubated in 99 ml of PBS with varied pH values (7.4, 6.0, and 5.0) under constant shaking. At designated time points (0.5, 2, 4, 6, 9, 12, and 24 hours), equal volume of PBS solution was withdrawn for UV-Vis test and replaced by an equal volume of fresh PBS buffer. To investigate the influence of NIR light on DATS release, the 808-nm NIR laser (1.0 W/cm^2) was used to irradiate the DATS release system for 10 min. According to the same above method, the release of Fe, Zn, and Gd ions from MSDG was measured by ICP-MS.

H_2S generation from MSDG

To detect the generation of H_2S from MSDG, equal amounts of MSDG (1 mg/ml, 1 ml) in dialysis membrane bags (M_w = 10,000) were immersed in 99 ml of PBS buffer (pH 7.4, 6.0, and 5.0) containing GSH (0, 2 mM) under constant shaking. The generation of H_2S was measured on the basis of a standard methylene blue method. Briefly, 1 ml of PBS buffer was withdrawn at designated time points (0.5, 2, 4, 6, 9, 12, and 24 hours), followed by addition of 1 ml of mixed solution of zinc acetate and sodium acetate (mass ratio = 4:1). The pellets were collected by centrifugation (13,000 rpm, 40 min) and redissolved by 500 μl of 1.2 M HCl solution of $FeCl_3$ (5 mg/ml) and *N*,*N*-dimethyl-*p*-phenylenediamine sulfate (1.4 mg/ml). After 20 min of incubation at 37°C, methylene blue was formed and measured at the absorbance of 665 nm. Then, the generation H_2S concentration was determined on the basis of a standard curve of Na_2S solution.

H_2S detection assay

After treatment with MSDG, H_2S in *E. coli* and MRSA biofilms was detected using a WSP-1 probe. Briefly, 15 μM WSP-1 was incubated with *E. coli* and MRSA biofilms in the dark for 30 min. After residual WSP-1 was removed, the samples were washed by PBS and then observed on an inverted fluorescent microscope (Nikon, ECLIPSE, Japan). Similar method was used to detect H_2S gas in the MSDG/macrophage incubation system.

In vitro cytotoxicity measurement

The cytotoxicity of MSDG against human umbilical vein fusion cells (EA.hy 926) was determined by the CCK-8 assay. For the CCK-8 assay, EA.hy 926 cells were cultured in DMEM with high glucose (DMEM-H), 10% fetal bovine serum (FBS), and 1.0% antibiotic-antimycotic at 37°C under a humidified 5% CO_2–containing atmosphere. Then, 200 μl of EA.hy 926 cell suspension was seeded in each well of 96-well plate. After 12 hours of wall-adherent growth, 200 μl of MSDG solutions with varied concentrations was added into each well for 24 hours of coincubation with EA.hy 926 cells. The Control group was added with 200 μl of sterile water. Last, 100 μl of CCK-8 dye was added into each well of the 96-well plate. After another 2 hours of incubation, the absorbance of each well at 450 nm was recorded by using an enzyme-labeled instrument (BioTek Epoch, USA). Cell viability (%) was calculated on the basis of the following formula (4)

$$\text{Cell viability} = \frac{OD_{Sample} - OD_{Control}}{OD_{Control}} \times 100\% \quad (4)$$

Cell viability without MSDG was set as the Control group.

Similar method was used for the evaluation of cell viability of RAW264.7 macrophages.

In addition, we also investigated the influence of NIR laser irradiation on the cell viabilities of EA.hy 926 and RAW264.7 cells when incubated with MSDG (30 μg/ml). The 808-nm NIR laser (1.0 W/cm^2) was used to irradiate the cells for 10 min.

In vitro antibiofilm activity

E. coli [American Type Culture Collection (ATCC) 35218] and methicillin-resistant *S. aureus* (MRSA, ATCC 43300) incubated in tryptic soy broth (TSB) media were used for evaluation of the therapeutic effects of different treatments against dense biofilm structures. Prepared bacterial suspensions (10^7 CFU/ml) were seeded in 96-well plates or confocal dishes for 48 hours of incubation at 37°C to form biofilms. Then, the biofilms were treated in the Control, NIR, MSG, MSG + NIR, MSDG, and MSDG + NIR groups, respectively. The concentrations of both MSG and MSDG in the groups of MSG, MSDG, MSG + NIR, and MSDG + NIR are 30 μg/ml. Around 10 min before NIR irradiation, MSG or MSDG solutions were applied to biofilms. The remaining biofilms at the bottom of 96-well plates were fixed with methanol and stained with crystal violet. Residual dye was washed by 30% ethylic acid, and the eluent was measured at a wavelength of 590 nm on an enzyme-labeled instrument (BioTek Epoch, USA). According to the spread plate method (SPM), the supernatants and biofilms were disrupted and dispersed in 1 ml of physiological saline, and then 10-fold diluted into a series of gradients. Last, 100 μl of dilutions was extracted and spread onto Columbia blood agar plates (CNA). After overnight incubation at 37°C, bacterial colonies on the plates were counted.

Evaluation of biofilm structure

E. coli and MRSA biofilms were established in confocal dishes. After different treatments, 500 μl of Syto9 (5.01 μM) was used to stain the biofilms in the dark for 30 min. The biofilm structure was observed on a confocal laser scanning microscope (CLSM; 510 Meta, Zeiss, Germany), and the Syto9 channel's relative fluorescence intensity of the biofilms was quantified on five different imaging areas by using an ImageJ/FIJI (https://imagej.nih.gov/ij/) software.

SEM observation

E. coli and MRSA biofilms were established. After different treatments, 2.5% glutaraldehyde was used to fix the biofilms at 4°C for 24 hours. Different gradients (30, 50, 70, 80, 90, 95, and 100%) of ethanol were used to dehydrate the biofilms at room temperature for 10 min. After freeze drying and platinum sputter coating, the samples were observed on a SEM system (JEOL JSM-6310LV, Japan).

gDNA level assay in solutions

The Bacterial DNA Extraction Kit (MolPure Bacterial DNA Kit, Yeasen) was used to extract the gDNA of bacteria. The extracted gDNA was dispersed in aqueous solution (2 mM GSH, pH 5.0). After the gDNA solutions were treated by MSG and MSDG at 37°C for 24 hours, the gDNA was collected by centrifugation. Subsequently, 1.0% tris-acetate-EDTA agarose gel electrophoresis and NA-Red (Nucleic Acid Red, Beyotime) staining were used to identify the gDNA cleavage products, and the gel was imaged with a Bio-Rad FX imaging system (USA).

Evaluation of eDNA in the biofilm

E. coli and MRSA biofilms were established in 48-well plates. After different treatments, biofilms in different groups were collected into 1-ml sterilized H_2O via two cycles of vortexing and sonication. Centrifugation (5000*g* for 10 min at 4°C) was used to separate bacterial cells from the EPS, and the supernatant liquids were collected. A 0.2-μm cellulose acetate filter was used to filter the supernatant liquids. Last, the concentration of eDNA was quantified with NanoDrop 2000c Spectrophotometer (Thermo Fisher Scientific). After different treatments, SYTOX (2 μM) solution was used to stain the eDNA in the biofilms in the dark for 40 min. After removing the residual dye via washing with PBS twice, CLSM was applied to observe the eDNA in the biofilms. The relative fluorescence intensity was quantified on five different imaging areas by using an ImageJ/FIJI (https://imagej.nih.gov/ij/) software.

ONPG hydrolysis assay

Treated biofilms were collected via vortexing and sonication for two cycles. The collected bacterial suspensions were incubated with the ONPG solution, and the absorbance of the mixed solution at 420 nm was recorded on an enzyme-labeled instrument (BioTek Epoch, USA).

Flow scatter diagrams of antibiofilm

Bacteria were collected by centrifugation at 5000 rpm for 5 min in a 2-ml Eppendorf tube. Then, 500 μl of Syto9 (FITC channel) and 500 μl of PI (PE channel) were added into the tube and incubated in the dark for 15 min. Afterward, the bacteria were washed and resuspended in fresh PBS and detected by BD FACSCanto II (USA).

Flow scatter diagrams of macrophages

RAW264.7 cells were seeded in several 12-well plates with a density of 1×10^5 cells per well. After incubation for 12 hours, 1 ml of DMEM-H containing 2 mM GSH with MSG or MSDG (30 μg/ml) was added into each well. After coincubation for another 24 hours, the RAW264.7 cells were scraped and collected by centrifugation (3000 rpm, 20 min). Then, the RAW264.7cells were resuspended in 100 μl of PBS containing 0.5 μg of allophycocyanin (APC)–labeled CD86 antibody and 1 μg of phycoerythrin (PE)–labeled CD206 antibody for 30 min of incubation in ice. Last, the CD86/CD206 expression on RAW264.7 macrophages was detected by BD FACSCanto II (USA).

Inflammatory-related gene expression by RT-qPCRs

RT-qPCRs were performed to evaluate the expression of genes in RAW264.7 macrophages on a QuanStudio 7 Flex system (Life Technologies) using the EZ-press RNA Purification Kit (EZBioscience, USA) to extract the total RNA and the Color Reverse Transcription Kit (EZBioscience, USA) to synthesize the complementary DNA. Then, SYBR Green qPCR Master Mix (EZBioscience) was chosen to detect the expression levels of the gene with three technical repeats. The primers used in the current study were provided in table S4. Gene quantification analysis was performed using the $2^{-\Delta\Delta Ct}$ method.

Cytokine secretion by ELISA

ELISA was used to detect the cytokine (IL-10 and IL-1β) concentration in different treated media. After incubating macrophages with MSG or MSDG for 24 hours, the media were collected and centrifuged to obtain the supernatants. Then, ELISA kits were used to detect the cytokine concentration.

Transwell migration assay

RAW264.7 cells (1×10^5 cells per well) were seeded in 8-μm transwell. The MSG or MSDG solutions were added into the lower chambers followed by coincubation for 24 hours. The cells on the bottom of the transwell were stained with crystal violet and counted under an optical microscope (Nikon, ECLIPSE, Japan).

Preparation of the macrophage-conditioned media

RAW264.7 cells (2×10^5 cells per well) were coincubated with MSG or MSDG in a six-well plate at 37°C for 1 day. Through centrifugation and filtration, the collected macrophage culture media were mixed with complete medium DMEM using the ratio of 1:2. Last, the above macrophage-conditioned media were stored at 4°C for further use.

Tube formation

EA.hy 926 cells (2×10^4 cells per well) were seeded into 96-well plates precoated with Matrigel matrix (BD, Corning, USA) and different macrophage-conditioned media at 37°C. After incubation for 6 hours, the cells were fixed and stained by calcein, and then the images were recorded using an inverted fluorescent microscope (Nikon, ECLIPSE, Japan). The number of junctions was counted using ImageJ/FIJI (https://imagej.nih.gov/ij/) software.

Scratch assay

EA.hy 926 cells (1×10^5 cells per well) were plated in 12-well plates and incubated at 37°C to form a confluent monolayer. Then, the monolayer cells were scraped with a pipette tip and washed three times using PBS. Next, the cells were coincubated with different macrophage-conditioned media (diluted using DMEM without FBS at a ratio of 1:2) at 37°C for 24 hours. For each group, removing media and washing by PBS, the scratch area was observed with an optical microscope (Nikon, ECLIPSE, Japan) and calculated using ImageJ/FIJI (https://imagej.nih.gov/ij/) software.

In vitro immunofluorescence staining of macrophages

RAW264.7 cells were seeded in several 12-well plates with a density of 1×10^5 cells per well. After the RAW264.7 cells were incubated with MSG or MSDG for 24 hours, the cells were fixed by 4% paraformaldehyde for 15 min at 4°C, washed with PBS three times, permeabilized with 0.2% Triton X-100 for 10 min, blocked for 15 min, and washed with PBS three times. Then, the cells were incubated with rabbit antibody against CD206 (1:500, Abcam) at 4°C overnight. After the cells were resuscitated at room temperature for 30 min and washed with PBS three times, Alexa Fluor 488–labeled goat anti-rabbit (1:500, Abcam) was added. Then, the cells

were incubated at room temperature in the dark for 1 hour and washed with PBS three times. DAPI was used to stain the nuclei. All images were captured with a fluorescent microscope (OLYMPUS, IX70, Japan).

Western blot analysis

The BCA protein assay kits were used to qualify the total concentration of protein. First, equivalent proteins were subjected to SDS–polyacrylamide gel electrophoresis and electrophoresed for 90 min at 120 V. Then, the proteins were transferred to polyvinylidene difluoride (PVDF) membranes at 100 V for 80 min. Afterward, the PVDF membranes were blocked for 2 hours and maintained at 4°C overnight with primary antibodies: glyceraldehyde-3-phosphate dehydrogenase (GAPDH) (BioTNT, Shanghai, China) and pAMPK (Cell Signaling Technology, Boston, MA, USA). Then, the PVDF membranes were incubated with secondary antibodies at room temperature for 1 hour. The P-ECL solutions (EpiZyme, Shanghai, China) were used for chemiluminescence measurement on a luminescent image analyzer (ImageQuant LAS 4000 mini). After washing with tris-buffered saline with Tween 20, the PVDF membranes were incubated with AMPK (Cell Signaling Technology, Boston, MA, USA) at room temperature for 2 hours. Later, the PVDF membranes were incubated with secondary antibodies at room temperature for 1 hour. Last, the P-ECL solutions and a luminescent image analyzer were used to detect chemiluminescence.

Animal experiment ethics

The animal experiment was approved by the Animal Ethical and Welfare Committee of University of Science and Technology of China Animal Department with an approval number of USTCACUC212101008. All handling and surgical procedures followed the approved guidelines.

Mouse implant–related infection model

BALB/c mice were purchased from the School of Agriculture and Biology, Shanghai Jiao Tong University for in vivo experiments. The mouse implant–related infection model was established and used to assess the antibiofilm abilities of six groups (Control, NIR, MSG, MSDG, MSG + NIR, and MSDG + NIR). Briefly, after intraperitoneal anesthesia in mice by 3% pentobarbital sodium, the mouse skin on the back was shaved, disinfected, and incised. The PEEK washers with pre-prepared biofilm were implanted at the back of neck, and then the wounds of skin were sutured immediately. Last, 200 μl of MSG and MSDG solutions (30 μg/ml) was applied in different treatments. There was an incubation time of about 10 min after injection and before NIR laser irradiation.

Microbiological and SPM evaluation

After surgery, the mice implantation sites were observed periodically at days 0, 5, 10, and 14 for grasping of their changes. All mice were euthanized at day 14. After surgery, the subcutaneous implants with the peripheral soft tissues were aseptically harvested. The collected PEEK washers were washed and immersed in 1 ml of PBS, followed by sonication and vortex to dislodge the adherent bacteria. Meanwhile, the corresponding peripheral soft tissues were weighed and homogenized in 1 ml of sterile PBS with a homogenizer. Last, the residual bacteria in the PEEK washers and corresponding peripheral soft tissues were evaluated by using SPM with three technical repeats for each group.

SEM observation of the PEEK washers collected from mice

After different treatments, the collected PEEK washers from mice in different groups were fixed using 2.5% glutaraldehyde at 4°C for 24 hours. Then, different gradients (30, 50, 70, 80, 90, 95, and 100%) of ethanol were used to dehydrate at room temperature for 10 min, respectively. After freeze drying for 8 hours and platinum sputter coating, the samples were observed on a SEM system (JEOL JSM-6310LV, Japan).

Histological observation

The soft tissues around the implants were fixed by formaldehyde and dehydrated with alcohol solutions, followed by paraffin wax embedding and slicing. Then, Leica SP1600 Microtome (Leica, Hamburg, Germany) was used for histological analyses. H&E and Giemsa staining were used for bacterial contamination assessment of the peripheral soft tissues under an optical microscope (OLYMPUS, IX70, Japan). Masson staining was used to evaluate the formation of collagen fiber after different treatments using an optical microscope (OLYMPUS, IX70, Japan). ImageJ/FIJI (https://imagej.nih.gov/ij/) software was used to quantify the data on three different imaging areas. All images were converted into binary ones with a fixed threshold to enable substrate comparison.

In vivo infrared thermal imaging

After the injection of MSG or MSDG solutions into the mice infectious sites, infrared thermal imagining camera was used to record the temperature change upon 808-nm laser irradiation.

In vivo H_2S release detection

After the injection of MSG or MSDG solutions into the infectious sites, H_2S probe (WSP-5) was used to detect H_2S release in vivo at the infectious sites on a small-animal imaging system (IVIS Spectrum, PerkinElmer).

In vivo MRI and PAI

Before and after injection of MSDG into the mice infectious sites, MRI and PAI were recorded on a 7.0-T Bruker BioSpec small-animal MRI system and Vevo LAZR PAI system, respectively.

Immunofluorescence and immunohistochemistry staining

Peripheral tissue sections at day 14 were harvested and immersed in paraformaldehyde solution. After dehydration, the samples were embedded in paraffin and made in sections for immunofluorescence staining of IL-6, TNF-α, CD206, iNOS, CD31, and α-SMA. All slides were observed and images were captured with a fluorescent microscope (OLYMPUS, IX70, Japan). Immunohistochemistry staining images of CD31 were observed under a fluorescent microscope (OLYMPUS, IX70, Japan).

Biosafety assessment

After scarification at the end of treatment, the major organs (heart, liver, spleen, lung, and kidney) were collected for H&E staining. Besides, the body weight of mice was also recorded during the treatment.

Statistical analysis

All data were shown as means ± SD.. Statistical analysis between two groups was performed by using Student's t test. $P < 0.05$ was

considered to be statistically significant. $n = 3$ to 5; means ± SD; n.s., no significant; $^{*}P < 0.05$, $^{**}P < 0.01$, $^{***}P < 0.001$, and $^{****}P < 0.0001$.

SUPPLEMENTARY MATERIALS

Supplementary material for this article is available at https://science.org/doi/10.1126/sciadv.abn1701

REFERENCES AND NOTES

1. E. O'Cearbhaill, Shedding light on implant-associated infection. *Sci. Transl. Med.* **11**, eaaz3709 (2019).
2. S. Wu, J. Xu, L. Zou, S. Luo, R. Yao, B. Zheng, G. Liang, D. Wu, Y. Li, Long-lasting renewable antibacterial porous polymeric coatings enable titanium biomaterials to prevent and treat peri-implant infection. *Nat. Commu.* **12**, 3303 (2021).
3. L. Tan, J. Fu, F. Feng, X. Liu, Z. Cui, B. Li, Y. Han, Y. Zheng, K. W. K. Yeung, Z. Li, S. Zhu, Y. Liang, X. Feng, X. Wang, S. Wu, Engineered probiotics biofilm enhances osseointegration via immunoregulation and anti-infection. *Sci. Adv.* **6**, eaba5723 (2020).
4. Y.-K. Wu, N.-C. Cheng, C.-M. Cheng, Biofilms in chronic wounds: Pathogenesis and diagnosis. *Trends Biotechnol.* **37**, 505–517 (2019).
5. J. W. Costerton, P. S. Stewart, E. P. Greenberg, Bacterial biofilms: A common cause of persistent infections. *Science* **284**, 1318–1322 (1999).
6. P. S. Stewart, J. William Costerton, Antibiotic resistance of bacteria in biofilms. *Lancet* **358**, 135–138 (2001).
7. S. E. Birk, A. Boisen, L. H. Nielsen, Polymeric nano- and microparticulate drug delivery systems for treatment of biofilms. *Adv. Drug Del. Rev.* **174**, 30–52 (2021).
8. D. Davies, Understanding biofilm resistance to antibacterial agents. *Nat. Rev. Drug Discov.* **2**, 114–122 (2003).
9. S. M. Hurtley, Biofilm formation from cell fountains. *Science* **369**, 45.15–45.47 (2020).
10. K. Schilcher, A. R. Horswill, Staphylococcal biofilm development: Structure, regulation, and treatment strategies. *Microbiol. Mol. Biol. Rev.* **84**, e00026-19 (2020).
11. K. P. Rumbaugh, K. Sauer, Biofilm dispersion. *Nat. Rev. Microbiol.* **18**, 571–586 (2020).
12. H. Koo, R. N. Allan, R. P. Howlin, P. Stoodley, L. Hall-Stoodley, Targeting microbial biofilms: Current and prospective therapeutic strategies. *Nat. Rev. Microbiol.* **15**, 740–755 (2017).
13. C. A. Fux, J. W. Costerton, P. S. Stewart, P. Stoodley, Survival strategies of infectious biofilms. *Trends Microbiol.* **13**, 34–40 (2005).
14. D. Hu, Y. Deng, F. Jia, Q. Jin, J. Ji, Surface charge switchable supramolecular nanocarriers for nitric oxide synergistic photodynamic eradication of biofilms. *ACS Nano* **14**, 347–359 (2020).
15. C. Tong, X. Zhong, Y. Yang, X. Liu, G. Zhong, C. Xiao, B. Liu, W. Wang, X. Yang, PB@PDA@Ag nanosystem for synergistically eradicating MRSA and accelerating diabetic wound healing assisted with laser irradiation. *Biomaterials* **243**, 119936 (2020).
16. D. Hu, H. Li, B. Wang, Z. Ye, W. Lei, F. Jia, Q. Jin, K.-F. Ren, J. Ji, Surface-adaptive gold nanoparticles with effective adherence and enhanced photothermal ablation of methicillin-resistant *Staphylococcus aureus* biofilm. *ACS Nano* **11**, 9330–9339 (2017).
17. S. Tian, L. Su, Y. Liu, J. Cao, G. Yang, Y. Ren, F. Huang, J. Liu, Y. An, H. C. van der Mei, H. J. Busscher, L. Shi, Self-targeting, zwitterionic micellar dispersants enhance antibiotic killing of infectious biofilms—An intravital imaging study in mice. *Sci. Adv.* **6**, eabb1112 (2020).
18. L. Hall-Stoodley, J. W. Costerton, P. Stoodley, Bacterial biofilms: From the natural environment to infectious diseases. *Nat. Rev. Microbiol.* **2**, 95–108 (2004).
19. C. Szabó, Hydrogen sulphide and its therapeutic potential. *Nat. Rev. Drug Discov.* **6**, 917–935 (2007).
20. J. L. Wallace, R. Wang, Hydrogen sulfide-based therapeutics: Exploiting a unique but ubiquitous gasotransmitter. *Nat. Rev. Drug Discov.* **14**, 329–345 (2015).
21. C. Szabó, H. Ischiropoulos, R. Radi, Peroxynitrite: Biochemistry, pathophysiology and development of therapeutics. *Nat. Rev. Drug Discov.* **6**, 662–680 (2007).
22. Y. Wang, T. Yang, Q. He, Strategies for engineering advanced nanomedicines for gas therapy of cancer. *Natl. Sci. Rev.* **7**, 1485–1512 (2020).
23. Z. Yuan, C. Lin, Y. He, B. Tao, M. Chen, J. Zhang, P. Liu, K. Cai, Near-infrared light-triggered nitric-oxide-enhanced photodynamic therapy and low-temperature photothermal therapy for biofilm elimination. *ACS Nano* **14**, 3546–3562 (2020).
24. S. Yu, G. Li, R. Liu, D. Ma, W. Xue, Dendritic Fe3O4@poly(dopamine)@PAMAM nanocomposite as controllable NO-releasing material: A synergistic photothermal and NO antibacterial study. *Adv. Funct. Mater.* **28**, 1707440 (2018).
25. Q. Gao, X. Zhang, W. Y. Yin, D. Q. Ma, C. J. Xie, L. R. Zheng, X. H. Dong, L. Q. Mei, J. Yu, C. Z. Wang, Z. J. Gu, Y. L. Zhao, Functionalized MoS_2 nanovehicle with near-infrared laser-mediated nitric oxide release and photothermal activities for advanced bacteria-infected wound therapy. *Small* **14**, e1802290 (2018).
26. Y. Li, X. Liu, B. Li, Y. Zheng, Y. Han, D.-f. Chen, K. W. K. Yeung, Z. Cui, Y. Liang, Z. Li, S. Zhu, X. Wang, S. Wu, Near-infrared light triggered phototherapy and immunotherapy for elimination of methicillin-resistant *Staphylococcus aureus* biofilm infection on bone implant. *ACS Nano* **14**, 8157–8170 (2020).
27. Z. Yuan, C. Lin, L. Dai, Y. He, J. Hu, K. Xu, B. Tao, P. Liu, K. Cai, Near-infrared light-activatable dual-action nanoparticle combats the established biofilms of methicillin-resistant *Staphylococcus aureus* and its accompanying inflammation. *Small* **17**, 2007522 (2021).
28. F. Benedetti, S. Curreli, S. Krishnan, S. Davinelli, F. Cocchi, G. Scapagnini, R. C. Gallo, D. Zella, Anti-inflammatory effects of H_2S during acute bacterial infection: A review. *J. Transl. Med.* **15**, 100 (2017).
29. M. Hoffman, A. Rajapakse, X. Shen, K. S. Gates, Generation of DNA-damaging reactive oxygen species via the autoxidation of hydrogen sulfide under physiologically relevant conditions: Chemistry relevant to both the genotoxic and cell signaling properties of H_2S. *Chem. Res. Toxicol.* **25**, 1609–1615 (2012).
30. J. Li, L. Xie, B. Li, C. Yin, G. Wang, W. Sang, W. Li, H. Tian, Z. Zhang, X. Zhang, Q. Fan, Y. Dai, Engineering a hydrogen-sulfide-based nanomodulator to normalize hyperactive photothermal immunogenicity for combination cancer therapy. *Adv. Mater.* **33**, 2008481 (2021).
31. J. Wu, A. Chen, Y. Zhou, S. Zheng, Y. Yang, Y. An, K. Xu, H. He, J. Kang, J. A. Luckanagul, M. Xian, J. Xiao, Q. Wang, Novel H_2S-releasing hydrogel for wound repair via in situ polarization of M2 macrophages. *Biomaterials* **222**, 119398 (2019).
32. L. Miao, X. Shen, M. Whiteman, H. Xin, Y. Shen, X. Xin, P. K. Moore, Y.-Z. Zhu, Hydrogen sulfide mitigates myocardial infarction via promotion of mitochondrial biogenesis-dependent M2 polarization of macrophages. *Antioxid. Redox. Signal.* **25**, 268–281 (2016).
33. C. R. Powell, K. M. Dillon, J. B. Matson, A review of hydrogen sulfide (H_2S) donors: Chemistry and potential therapeutic applications. *Biochem. Pharmacol.* **149**, 110–123 (2018).
34. C. M. Levinn, M. M. Cerda, M. D. Pluth, Activatable small-molecule hydrogen sulfide donors. *Antioxid. Redox. Signal.* **32**, 96–109 (2020).
35. G. A. Benavides, G. L. Squadrito, R. W. Mills, H. D. Patel, T. S. Isbell, R. P. Patel, V. M. Darley-Usmar, J. E. Doeller, D. W. Kraus, Hydrogen sulfide mediates the vasoactivity of garlic. *Proc. Natl. Acad. Sci. U.S.A.* **104**, 17977–17982 (2007).
36. D. Liang, H. Wu, M. W. Wong, D. Huang, Diallyl trisulfide is a fast H_2S donor, but diallyl disulfide is a slow one: The reaction pathways and intermediates of glutathione with polysulfides. *Org. Lett.* **17**, 4196–4199 (2015).
37. J. Li, X. Liu, L. Tan, Z. Cui, X. Yang, Y. Liang, Z. Li, S. Zhu, Y. Zheng, K. W. K. Yeung, X. Wang, S. Wu, Zinc-doped Prussian blue enhances photothermal clearance of *Staphylococcus aureus* and promotes tissue repair in infected wounds. *Nat. Commun.* **10**, 4490 (2019).
38. Y. Chen, Z.-H. Li, P. Pan, J.-J. Hu, S.-X. Cheng, X.-Z. Zhang, Tumor-microenvironment-triggered ion exchange of a metal-organic framework hybrid for multimodal imaging and synergistic therapy of tumors. *Adv. Mater.* **32**, 2001452 (2020).
39. E. Terreno, D. D. Castelli, A. Viale, S. Aime, Challenges for molecular magnetic resonance imaging. *Chem. Rev.* **110**, 3019–3042 (2010).
40. H. F. Zhang, K. Maslov, G. Stoica, L. V. Wang, Functional photoacoustic microscopy for high-resolution and noninvasive in vivo imaging. *Nat. Biotechnol.* **24**, 848–851 (2006).
41. Y. Liu, G. Wei, M. Ma, Y. Qiao, Role of acid in tailoring Prussian blue as cathode for high-performance sodium-ion battery. *Chem. A Eur. J.* **23**, 15991–15996 (2017).
42. Y. Zhu, B. Wang, Q. Gan, Y. Wang, Z. Wang, J. Xie, S. Gu, Z. Li, Y. Li, Z.-W. Ji, H. Cheng, Z. Lu, Selective edge etching to improve the rate capability of Prussian blue analogues for sodium ion batteries. *Inorg. Chem. Front.* **6**, 1361–1366 (2019).
43. A. Agrawal, S. H. Cho, O. Zandi, S. Ghosh, R. W. Johns, D. J. Milliron, Localized surface plasmon resonance in semiconductor nanocrystals. *Chem. Rev.* **118**, 3121–3207 (2018).
44. C. Avci, J. Ariñez-Soriano, A. Carné-Sánchez, V. Guillerm, C. Carbonell, I. Imaz, D. Maspoch, Post-synthetic anisotropic wet-chemical etching of colloidal sodalite ZIF crystals. *Angew. Chem. Int. Ed.* **54**, 14417–14421 (2015).
45. S. Gao, J. Hou, Z. Deng, T. Wang, S. Beyer, A. G. Buzanich, J. J. Richardson, A. Rawal, R. Seidel, M. Y. Zulkifli, W. Li, T. D. Bennett, A. K. Cheetham, K. Liang, V. Chen, Improving the acidic stability of zeolitic imidazolate frameworks by biofunctional molecules. *Chem* **5**, 1597–1608 (2019).
46. J. B. James, Y. S. Lin, Kinetics of ZIF-8 thermal decomposition in inert, oxidizing, and reducing environments. *J. Phys. Chem. C* **120**, 14015–14026 (2016).
47. T. Ubuka, Assay methods and biological roles of labile sulfur in animal tissues. *J. Chromatogr. B* **781**, 227–249 (2002).
48. G. L. Newton, M. Rawat, J. J. La Clair, V. K. Jothivasan, T. Budiarto, C. J. Hamilton, A. Claiborne, J. D. Helmann, R. C. Fahey, Bacillithiol is an antioxidant thiol produced in Bacilli. *Nat. Chem. Biol.* **5**, 625–627 (2009).
49. C. B. Whitchurch, T. Tolker-Nielsen, P. C. Ragas, J. S. Mattick, Extracellular DNA required for bacterial biofilm formation. *Science* **295**, 1487 (2002).
50. Z. Chen, H. Ji, C. Liu, W. Bing, Z. Wang, X. Qu, A multinuclear metal complex based DNase-mimetic artificial enzyme: Matrix cleavage for combating bacterial biofilms. *Angew. Chem. Int. Ed.* **55**, 10732–10736 (2016).
51. M. Okshevsky, R. L. Meyer, The role of extracellular DNA in the establishment, maintenance and perpetuation of bacterial biofilms. *Crit. Rev. Microbiol.* **41**, 341–352 (2015).

52. Z. Yuan, B. Tao, Y. He, C. Mu, G. Liu, J. Zhang, Q. Liao, P. Liu, K. Cai, Remote eradication of biofilm on titanium implant via near-infrared light triggered photothermal/photodynamic therapy strategy. *Biomaterials* **223**, 119479 (2019).
53. L. Tan, J. Li, X. Liu, Z. Cui, X. Yang, S. Zhu, Z. Li, X. Yuan, Y. Zheng, K. W. K. Yeung, H. Pan, X. Wang, S. Wu, Rapid biofilm eradication on bone implants using red phosphorus and near-infrared light. *Adv. Mater.* **30**, 1801808 (2018).
54. D. M. Mosser, K. Hamidzadeh, R. Goncalves, Macrophages and the maintenance of homeostasis. *Cell. Mol. Immunol.* **18**, 579–587 (2021).
55. X. Zhou, X. Chu, D. Xin, T. Li, X. Bai, J. Qiu, H. Yuan, D. Liu, D. Wang, Z. Wang, L-cysteine-derived H_2S promotes microglia M2 polarization via activation of the AMPK pathway in hypoxia-ischemic neonatal mice. *Front. Mol. Neurosci.* **12**, 58 (2019).
56. X. Zhou, Y. Cao, G. Ao, L. Hu, H. Liu, J. Wu, X. Wang, M. Jin, S. Zheng, X. Zhen, N. J. Alkayed, J. Jia, J. Cheng, CaMKKβ-dependent activation of AMP-activated protein kinase is critical to suppressive effects of hydrogen sulfide on neuroinflammation. *Antioxid. Redox. Signal.* **21**, 1741–1758 (2014).
57. R. Mounier, M. Théret, L. Arnold, S. Cuvellier, L. Bultot, O. Göransson, N. Sanz, A. Ferry, K. Sakamoto, M. Foretz, B. Viollet, B. Chazaud, AMPKα1 regulates macrophage skewing at the time of resolution of inflammation during skeletal muscle regeneration. *Cell Metab.* **18**, 251–264 (2013).
58. W. Ye, J. Wang, D. Lin, Z. Ding, The immunomodulatory role of irisin on osteogenesis via AMPK-mediated macrophage polarization. *Int. J. Biol. Macromol.* **146**, 25–35 (2020).
59. Z. Tu, M. Chen, M. Wang, Z. Shao, X. Jiang, K. Wang, Z. Yao, S. Yang, X. Zhang, W. Gao, C. Lin, B. Lei, C. Mao, Engineering bioactive M2 macrophage-polarized anti-inflammatory, antioxidant, and antibacterial scaffolds for rapid angiogenesis and diabetic wound repair. *Adv. Funct. Mater.* **31**, 2100924 (2021).
60. M. Benoit, B. Desnues, J.-L. Mege, Macrophage polarization in bacterial infections. *J. Immunol.* **181**, 3733–3739 (2008).

Acknowledgments: We acknowledge the Public Platform of State Key Laboratory of Natural Medicines for the use of analytical instrumentation facilities (FUJIFILM VisualSonics Vevo LAZR) and also thank Li Guo for her assistance in taking images. **Funding:** This study was supported by the National Natural Science Foundation of China (82102586, 81871788, and 81802181), the China Postdoctoral Science Foundation (2020 M671893), the Fundamental Research Funds for the Central Universities (WK9110000155), the Natural Science Foundation of Anhui Province, Distinguishing Youth Project (2108085 J41), the Key Research and Development Projects of Anhui Province (202004j07020013), the Anhui Provincial Postdoctoral Science Foundation (2019B302), and the Scientific Research Fund of Anhui Education (2020jyxm2316). **Author contributions:** Z.S., J.W., W.F., and C.Z. conceived and designed the concept of the experiments. Z.S. and W.F. synthesized the materials. Z.S., Z.Q., Q.L., and W.F. conducted the material characterizations. Z.S., L.K., J.W., J.M., Y.D., and J.T. conducted and analyzed most of the in vitro and in vivo experiments. Z.S., J.W., W.F., and C.Z. provided important experimental insights and cowrote the paper. Y.M., Y.D., and S.J. helped to do the magnetic resonance imaging experiments. All authors discussed, commented, and agreed on the manuscript. **Competing interests:** The authors declare that they have no competing interests. **Data and materials availability:** All data needed to evaluate the conclusions in the paper are present in the paper and/or the Supplementary Materials.

Submitted 9 November 2021
Accepted 16 February 2022
Published 8 April 2022
10.1126/sciadv.abn1701